

Chapter 2. SAR Imaging of the Ocean Surface

Benjamin Holt

Jet Propulsion Laboratory, California Institute of Technology, Pasadena CA USA

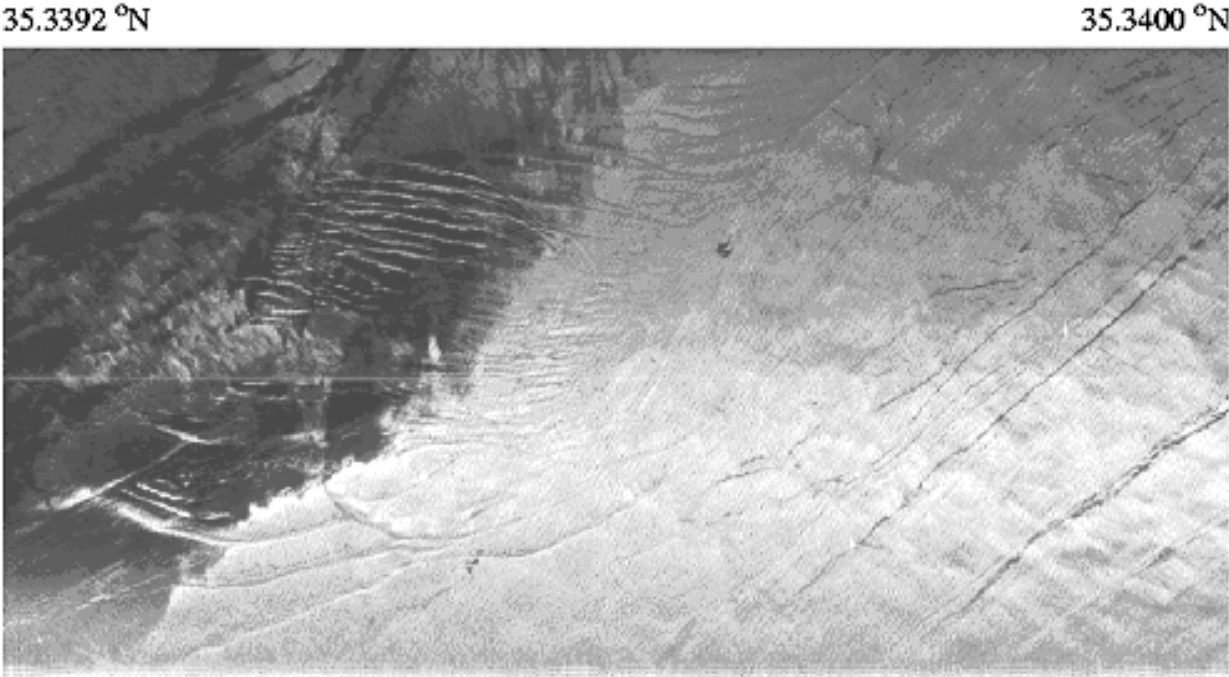
2.1 Introduction

The finely-detailed imagery of the ocean's surface from a synthetic aperture radar (SAR) is assuredly the most complex and least understood data set that is provided by a remote sensing instrument. What to make of the unprecedented two-dimensional views of waves, currents and eddies, slicks, surface manifestations of subsurface features, all brushed over by interactions with the boundary layer, have captivated and perplexed researchers for over three decades. Add to this mix the ocean's motion during the SAR imaging process and one has quite a challenge to derive quantitative information on what these image patterns uniquely provide on upper ocean processes and air-sea exchange. My son once observed that "It sounds like the ocean is laughing at us." When it comes to interpreting the complexities of SAR imagery of the ocean surface, it often feels like both the ocean and the SAR are laughing at us as we try to sort things out.

A SAR, operating from a satellite or aircraft, transmits radar signals and receives backscattered returns whose levels are directly dependent on the roughness of the ocean's surface. The characteristic frequencies of most SAR sensors (0.4 to 10 GHz, equivalent to 3 to 75 cm, and designated by X-, C-, S-, L-, and P-bands) are not commonly scattered from or bounced between air and water droplets, enabling the SAR signals to generally pass unchanged down and back through clouds. A SAR achieves its fine resolution (nominally 25 to 50 m for spaceborne systems) through its side-looking geometry, by precisely tracking the transmission and return of its short radar pulses, and detecting small Doppler shifts in the return signals that result from the SAR's motion past a point on the surface. The radar return is a complex interaction of the transmitted signal, whose characteristics are determined by the radar's frequency, polarization, and viewing geometry, and the illuminated surface, whose characteristics depend on roughness characteristics, electrical properties, and material composition.

Over the ocean, the radar return comes from roughness components that are approximately of similar wavelength or scale as the radar wavelength. The roughness components are wind-generated short waves that range from capillary to short gravity waves (wavelengths between a few to a few tens of centimeters and periods less than one second). Longer gravity waves and currents modulate the short wave field in ways that produce characteristic patterns on the radar imagery which reveal the presence of features. Understanding these patterns and deriving useful information from SAR about the ocean requires an understanding of the ocean interactions themselves as well as the interactions of the radar waves with the moving ocean.

The ocean features commonly seen on SAR imagery include surface waves, mesoscale ocean circulation structures such as eddies and currents, oily slicks, and surface manifestations of ocean dynamics present below the surface including internal waves and currents passing over shallow shoals. The SAR is so sensitive to the interaction of wind with the ocean surface that, in addition to wind speed, patterns and structures within the atmospheric boundary layer produce identifiable surface imprints. In some sense, wind is the master control switch in



35.2330°N 75.1765°W 5 km 35.2338°N 74.9335°W

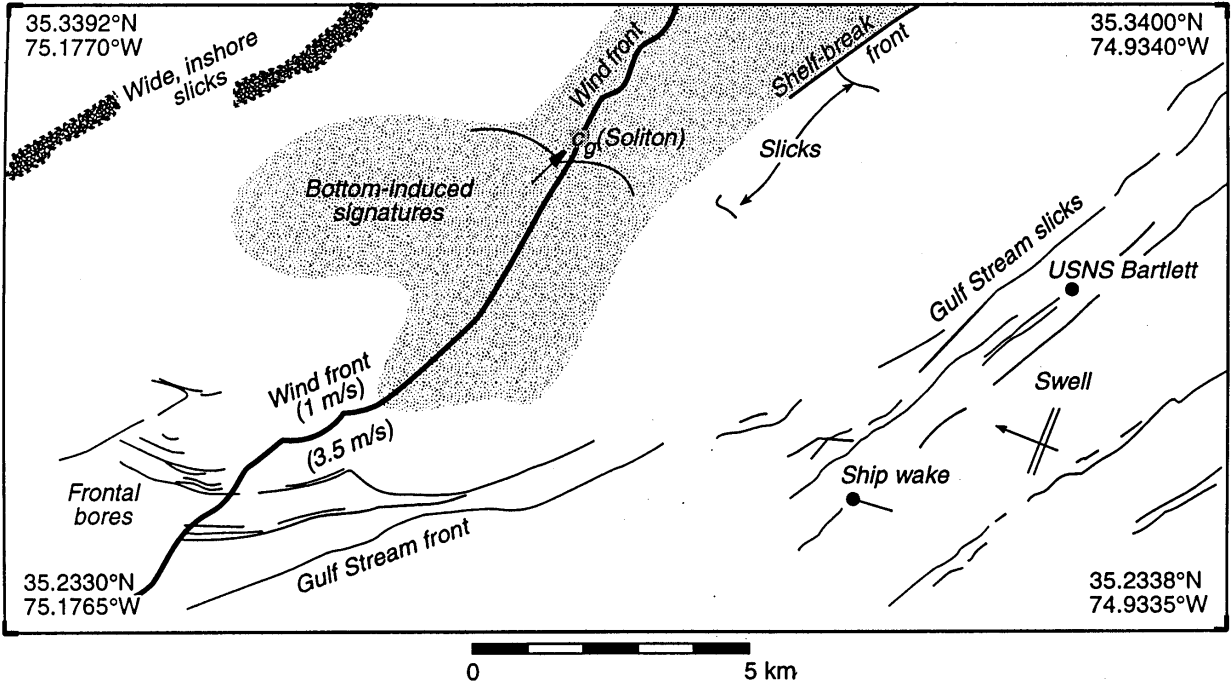


Figure 2.1. (a) Aircraft L-band VV SAR image that includes the north wall of the Gulf Stream and adjacent shelf near Cape Hatteras, (b) Sketch map of detectable features and conditions in (a) including the USNS Bartlett. [After Lyzenga and Marmorino, 1998]

terms of what is detected on radar imagery. High winds disperse the identifiable interactions of waves and currents, air and sea, or oil and sea that reveal most of the features. On the other hand, winds must reach above a threshold speed to sufficiently roughen the ocean surface so that a signal can be detected above the noise level of the instrument.

Figure 2.1 is a rather amazing example of SAR ocean imagery because of the number of identifiable features contained within a single frame [from *Lyzenga and Marmorino, 1998*]. Comparing the fine resolution (6.4 m) aircraft image with the schematic, one can see the bright shear boundary of the Gulf Stream front, the periodic pattern of swell propagating westward through the current field, periodic bright lines of internal waves ('bottom-induced signatures' and 'soliton') and frontal bores over the shelf, dark slicks both within the Gulf Stream and inshore, and a wind front separating the dark shelf water from the brighter Gulf Stream water. As we will see, the bright shear boundary and internal waves result from essentially the piling-up of short-waves in convergence zones; the dark slicks are produced by oil and weeds which dampen the short-wave field; and the dark shelf and bright current field result from the cold/warm temperatures of the adjacent shelf/Gulf Stream that affect the stability of the boundary layer which leads to a reduction of the wind speed on the shelf side. Lastly, the bright returns from two ships are indicated, with one ship stationary and the other in motion as shown by its stern wake.

What we have learned about spaceborne SAR imaging of the ocean surface comes from an initially intermittent but now continuous data record. The first spaceborne SAR was flown on NASA's SEASAT during 1978, being an L-band system operating at a single polarization of horizontal transmit-horizontal receive (HH) and a fixed 100-km swath with incident angles of between 20° and 26°. In addition to the anticipated observations of surface and internal waves seen before SEASAT from limited airborne SAR systems [e.g., *Elachi and Apel, 1976; Elachi, 1978; Elachi et al., 1977, and Elachi and Brown, 1977*], SEASAT SAR imagery revealed a number of features if not for the first time, at least the most extensively [e.g., *Vesecky and Stewart, 1982; Beal et al., 1981, 1983, 1986; Fu and Holt, 1982, 1983, 1984; Apel and Gonzalez, 1983*], including current boundaries, eddies over a wide range of scales (10 to 400 km), temperature fronts, shoaling bathymetry, and atmospheric patterns related to storms, roll vortices and rain cells. The next spaceborne SARs were flown on the space shuttle, including NASA's Shuttle Imaging Radar-A (SIR-A) in 1981, a single channel L-band HH SAR with optical data recording, and SIR-B in 1984, a digital single channel L-band HH SAR but with variable incident angles. The limited coverage provided distortion-free imaging of ocean waves (due to lower orbital altitudes of the shuttle compared to satellites), particularly from SIR-B, which was invaluable for validating wave imaging models developed from SEASAT data [e.g., *Alpers, 1983b; Hasselmann et al., 1985; Alpers and Bruening, 1986; Holt, 1988; Beal, 1991*].

The next spaceborne SAR was the European Space Agency's (ESA) ERS-1 mission in 1991, a C-band vertical transmit-vertical receive (VV) polarization SAR with a SEASAT-like 100-km swath and a range of incident angles between 20° and 26°. This highly successful mission was continued in 1995 with ERS-2, which as of 2003 continues to operate. The Japanese Space Agency flew the L-band HH JERS-1 SAR from 1992 to 1998. The JERS-1 SAR produced limited useful ocean imagery because of its land-oriented fixed incident angles of 32° to 38°. In between ERS-1 and JERS-1, the joint NASA/German Space Agency/Italian Space Agency mission, Shuttle Imaging Radar-C/X-band SAR (SIR-C/XSAR), flew twice in 1994. This three frequency (L/C/X bands), fully polarimetric system (HH/VV/HV/VH for L/C, and HH for X) provided the most extensive multi-parameter ocean data available to this day [*Holt, 1998*].

The next mission, the Canadian Space Agency's RADARSAT-1, a C-band HH system available at varying incident angles and swath widths (40 to 500 km), was launched in 1995 and as of 2004, continues to provide invaluable imagery. ESA's ENVISAT, launched in March 2002, carries a C-band dual polarization system with swath widths varying between 100 and 400 km.

This chapter provides an overview of the fundamental concepts of SAR imaging of the ocean surface along with examples of characteristic features seen and studied in the imagery, concepts that will be reemphasized in the more detailed following chapters. In addition, readers are encouraged to consider more rigorous explanations of SAR imaging found in several valuable books [*Ulaby et al.*, 1982, 1986; *Stewart*, 1985; *Apel*, 1987; *Elachi*, 1988; *Raney*, 1998]. In this chapter, the following questions will be considered: What is a SAR detecting on the ocean surface? What is the physical basis of the interaction of radar waves with the ocean surface? What are the characteristics of the types of features that are detected, under what range of conditions are they imaged, and what information can be extracted from these features? What are the differences in ocean feature detection that result from varying SAR instrument properties? How can one best make use of this imagery, particularly in combination with other remote sensing instruments? The chapter will conclude with a few examples of rather complicated images to 'walk through' the possible interpretations of what is being seen, and some features that still remain largely unexplained, to emphasize that there is still much to be learned from this captivating imagery, from the extensive data archives as well as with the continually improving SAR sensors currently operating and that will launch in the future.

2.2 The Ocean Surface and Radar Scattering

The ocean surface is where nearly all exchanges of heat, momentum, light, water, and gases between the atmosphere and the ocean take place. Most of the standard ocean remote sensing instruments detect only the ocean surface, including radar altimeters (sea surface height), radar scatterometers and SAR (radar backscatter), and both infrared and microwave radiometers (brightness temperature). The only exception is ocean color-type instruments that detect water-leaving spectral radiance in the visible bands. To understand each of these data sets requires consideration of how the ocean surface is interacting with both the upper ocean properties and the atmosphere.

Over the ocean, a SAR image consists of a fine resolution, two-dimensional radar backscatter map of the roughness of the ocean surface. The ocean radar return is controlled by the 1) dielectric constant, 2) roughness of the sea surface, 3) interaction of waves at different scales, 4) interaction of waves and currents, and 5) the intermediary presence of oils on the surface. For active microwave sensors, ocean roughness is comprised of the mean surface slope, dominated by the long-wavelength field, and the short-scale waves that range between capillary and short-gravity waves.

The standard formalism is that the reflectivity or brightness of the radar return, termed the normalized radar cross section or backscatter coefficient (σ^0 or 'sigma naught'), is the average level of incident energy, σ , scattered back to the antenna over a specified area, A (in m^2) on the ground. Sigma naught is a dimensionless quantity given in decibels (dB), where

$$\sigma^0 = 10 \log_{10} (\sigma / A). \quad (1)$$

SAR Imaging of the Ocean Surface

In addition to the physical and electrical properties and local slope of the reflected medium, the value of σ^0 depends on the radar system characteristics including frequency, polarization, and viewing or incident angles.

At common SAR incident angles between 20° and 60° (as referenced from nadir), the ocean roughness that SAR is most sensitive to arises from the ocean's short wave field on scales shorter than the SAR resolution cell and approximately similar to the SAR frequency (where frequency, f , and wavelength, λ_0 , are related by $\lambda_0 = c / f$, with c the speed of light). To first order these waves arise from local wind stress. The radar backscatter depends on the wavelength, orientation, and tilt of the waves in relation to the SAR. In the absence of wind, the surface will be largely smooth and hence specular, reflecting the radar energy away from the sensor. Increasing wind speeds will result in increasing ocean roughness and, hence, increased backscatter as more energy is returned back to the antenna. Longer waves, including both swell and internal waves, underlying currents, temperature fronts, and atmospheric features will cause a tilting as well as redistribution of the short wave field into characteristic patterns that are identifiable on SAR imagery. Thus the key to understanding a SAR ocean image is to make sense of what these surface patterns are revealing about the underlying ocean and overlying atmosphere.

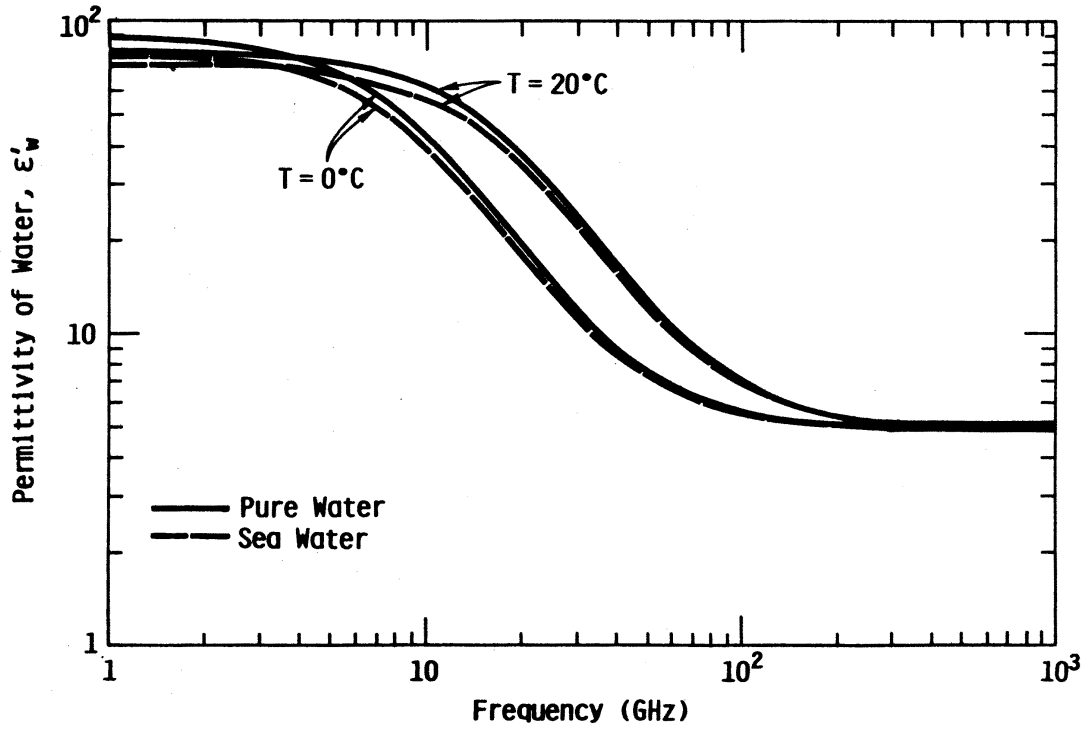
2.2.1 Dielectric Constant and Penetration Depth

Before delving into the general concepts of the ocean surface, radar scattering, and features, it is key to understand that the SAR microwaves do not penetrate beyond a few millimeters of the topmost layer or microlayer of the ocean surface. Thus, even though we may discuss using SAR to study features that occur at depths below this layer, such as internal waves, currents, and bathymetry, these features are only seen from SAR because of the interaction of the underlying current field associated with these features with the surface short wave field. To first order, whether or not radar waves penetrate into any medium is controlled by the dielectric constant of the particular medium. The dielectric constant characterizes a medium's response to the presence of an electric field. Thus radar waves impinging with water, ice or rain, in our discussion, will change the activity of charged molecules in ways that depend on the medium's properties. The dielectric constant, or complex permittivity ϵ_c , is described as

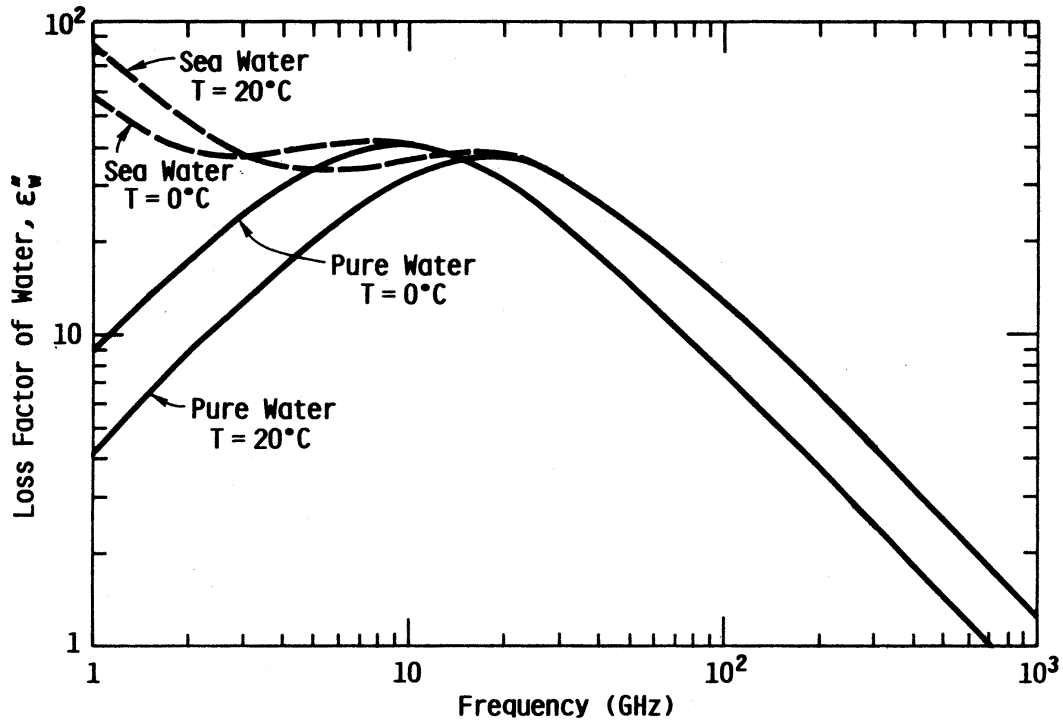
$$\epsilon_c = \epsilon' - i\epsilon'' \quad (2)$$

where ϵ' is the real part and ϵ'' is the imaginary part where $i = \sqrt{-1}$. The real part, ϵ' , often referred to as the dielectric constant, describes the ability of a medium to store electrical energy. The imaginary part, ϵ'' , commonly termed the loss factor, describes the electromagnetic loss of the medium. The loss tangent, $\tan \delta = \epsilon''/\epsilon'$, describes whether the material is a good conductor (large loss tangent $\tan \delta \gg 1$) or poor conductor (low loss tangent $\tan \delta \ll 1$).

As seen in Figure 2.2, particularly over the range of radar frequencies common to most SAR systems (1 to 10 GHz), fresh water has both a high permittivity ($\epsilon' > 40$) and a comparatively high loss ($\epsilon'' > 4$) due to the high polarity of the water molecule; thus, it is a good conductor. The addition of salt slightly reduces ϵ' but significantly increases ϵ'' . When sea water freezes, the dielectric constant is greatly reduced, as the free rotation of the polar water molecules is impeded, with sea ice typical values for ϵ' of 3 to 5 and ϵ'' of 0.1 to 1.0. Rain in the atmosphere, whether the droplets are frozen or unfrozen, effectively increases the dielectric

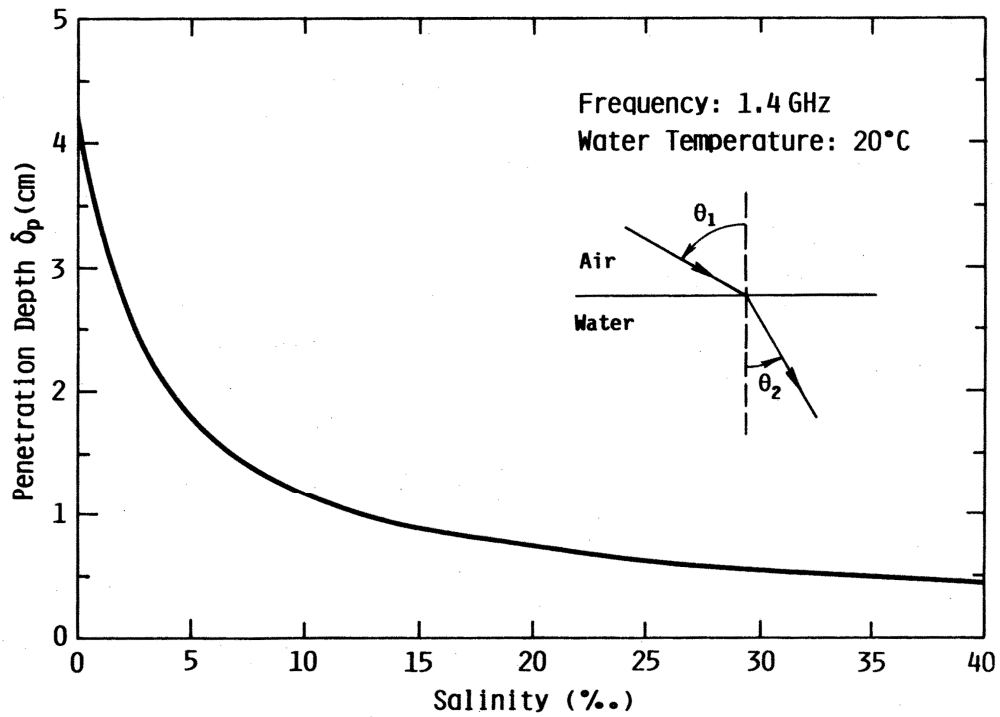


(a)

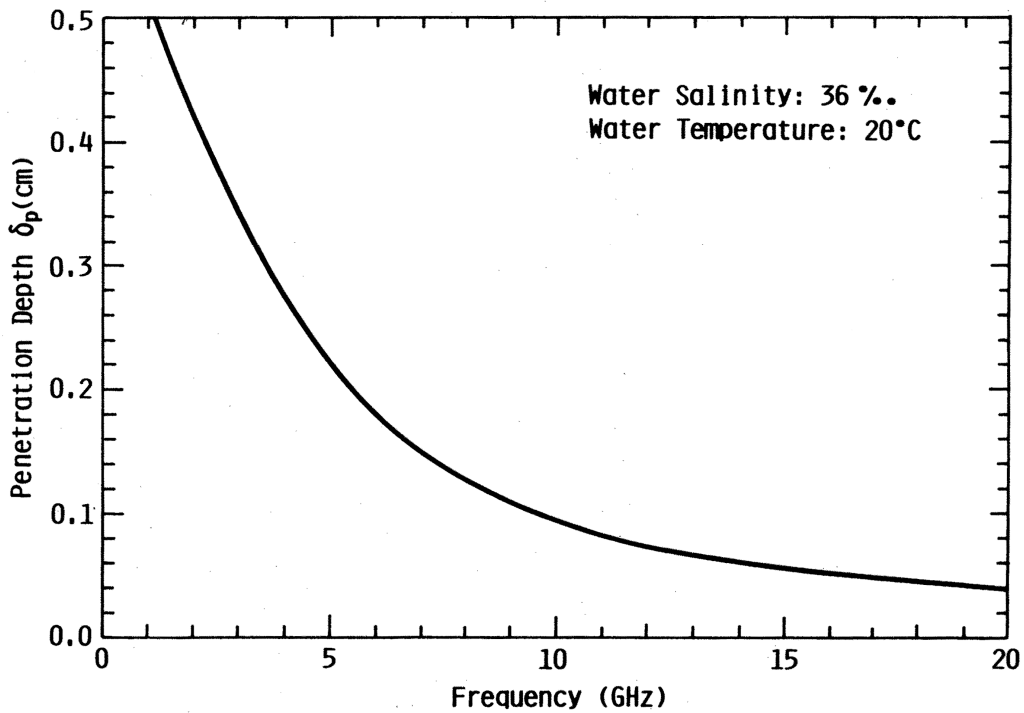


(b)

Figure 2.2. (a) Real and (b) imaginary parts of the complex dielectric constant of pure water and sea water over varying frequency and for 0°C and 20°C . Salinity of sea water $S = 32.45$ ‰ (salinity units). [After *Ulaby et al.*, Vol. III, 1986, Figure E.1]



(a) δ_p Versus Salinity



(b) δ_p Versus Frequency

Figure 2.3. Penetration depth of water (cm) as a function of (a) salinity at 1.4 GHz and (b) frequency at 36 ‰ (salinity units). [After *Ulaby et al.*, Vol. III, 1986, Figure 18.4]

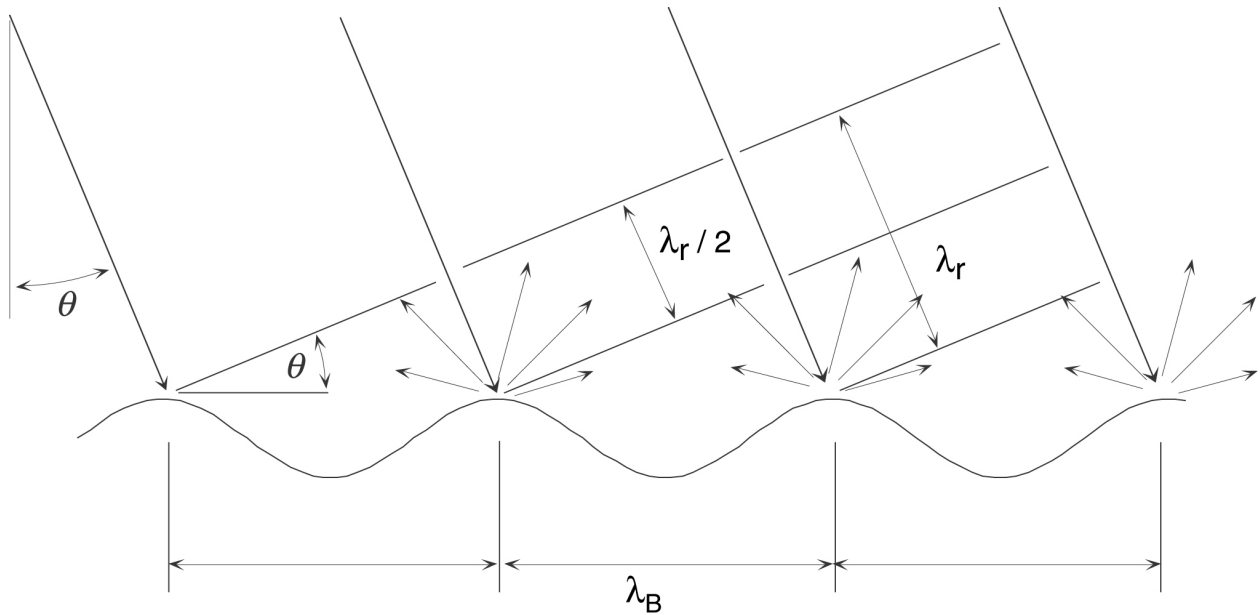


Figure 2.4. Illustration of Bragg scattering, where λ_r is the radar wavelength, λ_B is the sea surface wavelength, and θ is the local angle of incidence. [Adapted from *Martin*, 2004]

constant, resulting in increased scattering as well as reduced penetration through the atmosphere. A high dielectric medium (e.g., ocean) will have lower backscatter than a low dielectric medium (e.g., sea ice), because the increased penetration that occurs with a low loss medium generally results in an additional contribution from volume scattering.

The penetration depth, δ_p , of microwaves into a medium (attenuation of power to a certain level) depends on both radar wavelength, λ_r , and the loss tangent, as

$$\delta_p = \lambda_r / (2\pi \sqrt{\epsilon'} \tan \mathbf{d}). \quad (3)$$

Over the frequency range of 1 to 10 GHz (wavelengths of 3 to 23 cm), the penetration depth of ocean water is on the order of 0.1 to 1.0 cm (Figure 2.3), which for high conductivity materials like water is also termed skin depth. For sea ice, a poor conductor/low-loss medium, the penetration depth may be on the order of several radar wavelengths or even more. For more rigorous discussions on dielectric constants and penetration depth, refer to *Ulaby et al.* [1982, 1986], *Raney* [1998], and *Apel* [1987].

2.2.2 Ocean Surface Roughness

The SAR backscatter from the ocean within characteristic SAR incident angles ($\sim 18^\circ$ to 50°) in the absence of long waves is primarily due to Bragg or resonance scattering. This form of scattering also applies to land surfaces and sea ice. Under Bragg scattering (Figure 2.4), the incident radar waves are backscattered by the wind-generated, freely-propagating, short wave components of the ocean surface, λ_B , whose wavelengths are similar to the radar frequency, λ_r , using the follow relation:

$$\lambda_B = \lambda_r / 2 \sin \theta \quad (4)$$

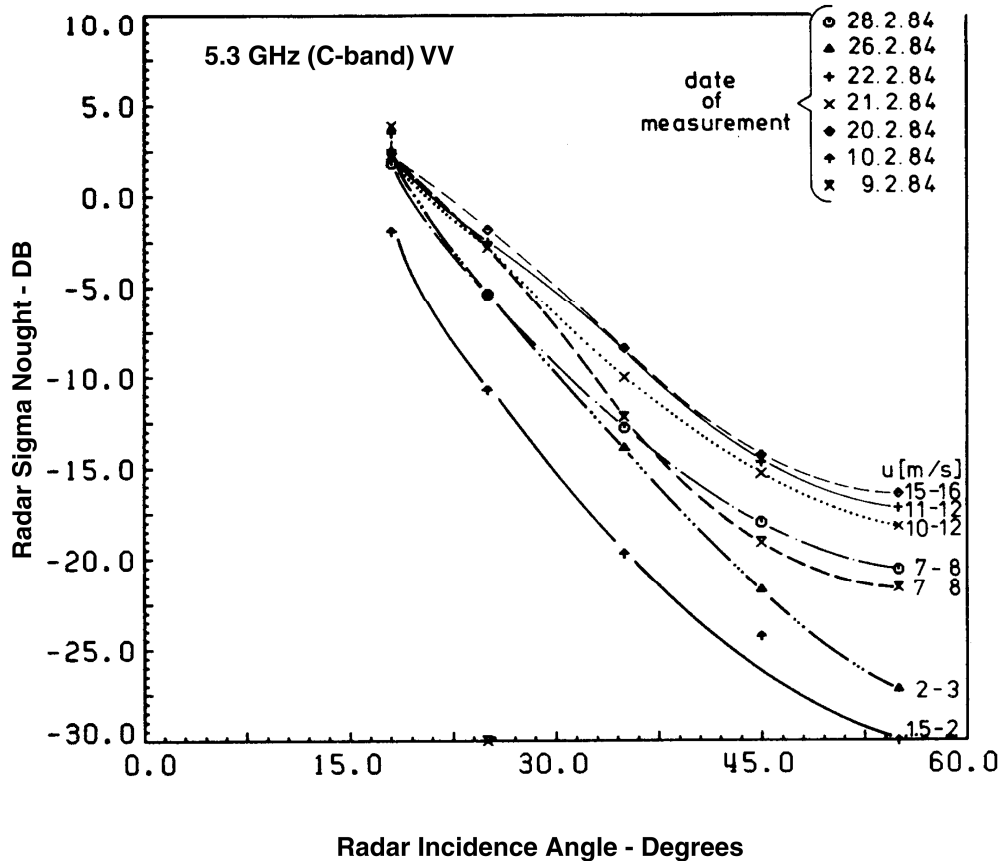


Figure 2.5. C-band (5.3 GHz) VV radar backscatter for varying wind speeds averaged over all azimuth angles as a function of incident angle. Each symbol represents data points of a specific flight day. [After Feindt et al., 1986]

where θ is the radar incident angle, the angle between the radar line-of-sight, and the local vertical. This results in a coherent addition (resonance) of returns from adjacent waves that are in phase, which is strongest when the Bragg waves are traveling towards or away from the radar look direction, in fact at quite a narrow range of angles [Plant, 1990]. As wind-waves are usually continuously distributed in wavelength, resonant waves are commonly present and with components moving in the required direction, so the conditions for Bragg scattering are generally met. Bragg scattering is prevalent between incident angles of 15° and 70° [e.g., Valenzuela, 1978]. For angles less than 15° , scattering primarily occurs through specular reflection (smooth surfaces oriented perpendicular to antenna look direction), while for angles larger than 70° , scattering from the sides of the waves (wedge scattering) is most prevalent.

For a characteristic range of SAR incident angles (20° to 26°), Bragg waves have the following values for common SAR frequencies: for X-band (3 cm), 3.9 ± 0.5 cm; for C-band (5.5 cm), 7 ± 1 cm; and L-band (23 cm), 30 ± 4 cm. Note from (4) that λ_B decreases with increasing incident angle. Under low winds, a threshold wind speed must be reached before Bragg waves are generated at the appropriate scale required to produce a measurable radar return. This is shown to some degree in Figure 2.1 in the shelf water region and later in Figure 2.12c, showing very patchy response across areas of variable low winds. The threshold wind speeds for X-, C-, and L-bands at 20° incident angles are approximately the following: 2.5, 2.2, and 2.0 m s^{-1} ,

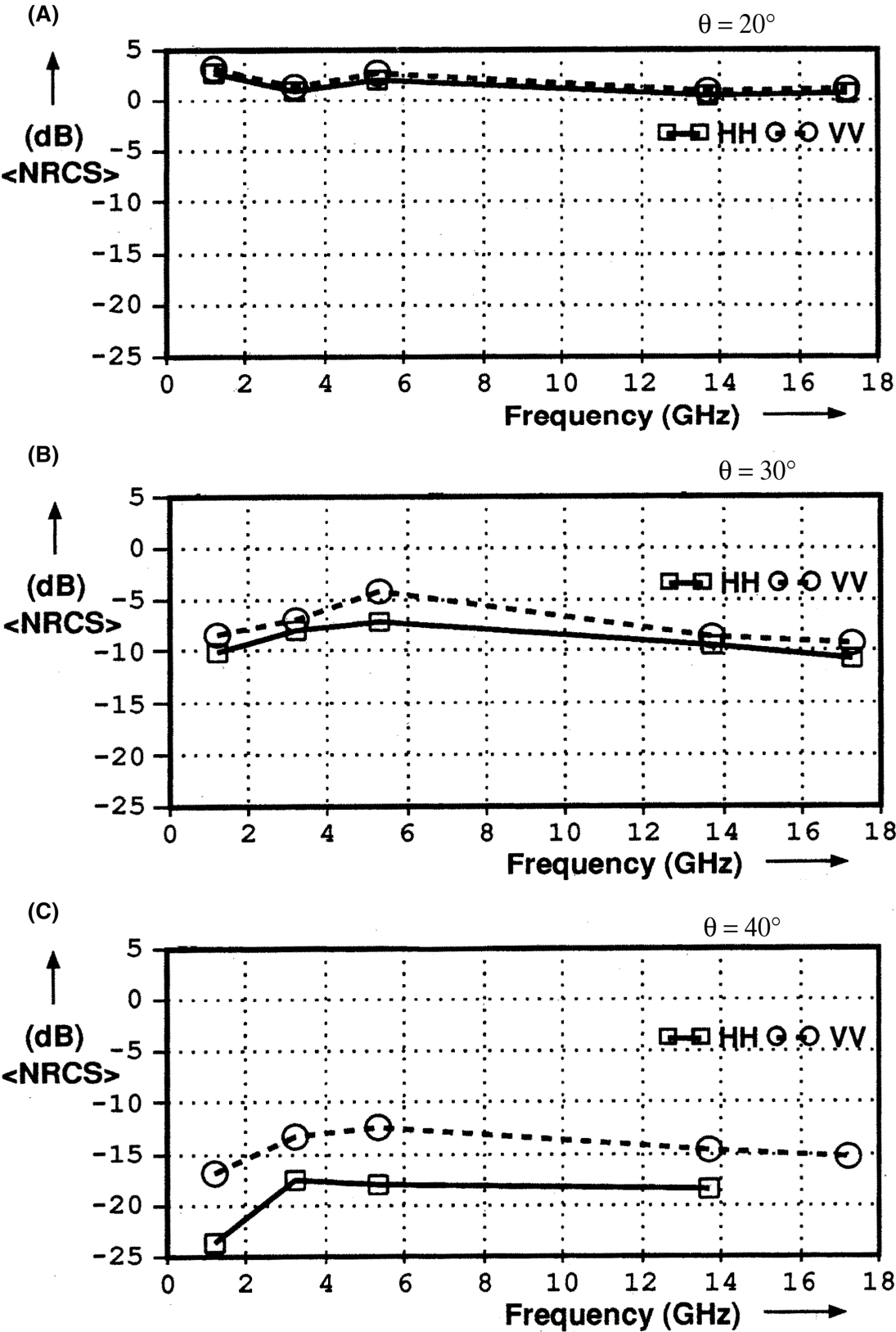


Figure 2.6. Average radar backscatter for range of frequency from 1 to 18 GHz at HH and VV polarizations and varying incident angles of (a) 20° , (b) 30° , and (c) 45° , for a fixed wind speed of 10 m s^{-1} . [After Unal et al., 1991]

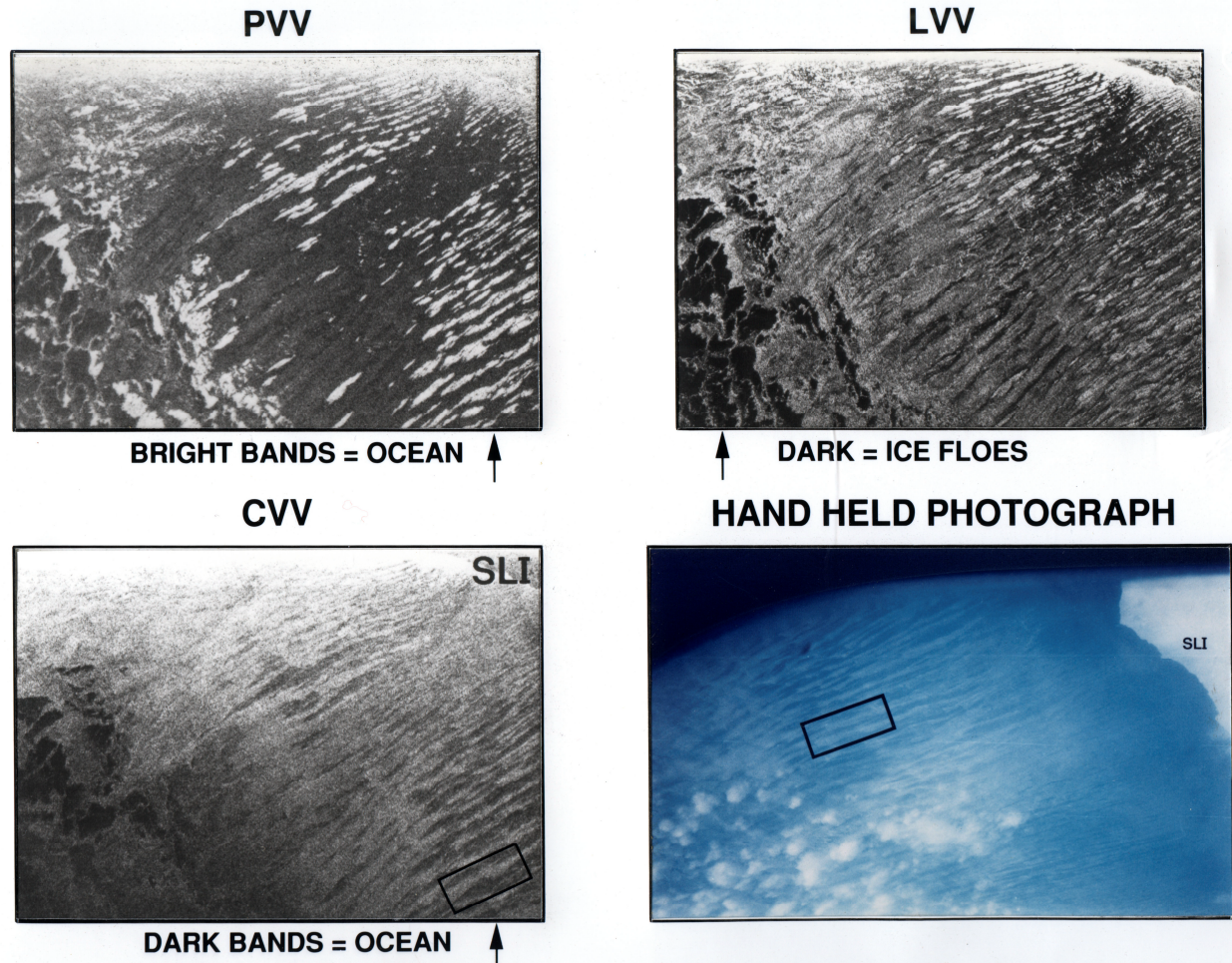


Figure 2.7. Images of sea ice in the St. Lawrence Island polynya taken from the NASA DC-8 overflight on 22 March 1988. The multi-frequency fully polarimetric SAR images were obtained simultaneously and examples are shown at P-band VV, L-band VV, and C-band VV. Each SAR image covers an area of 6 km by 8 km. The long axes of these images are parallel to the flight path, while the image white-out at the top of each image is due to nadir saturation of the radar. A hand-held photograph of the polynya provides identification of ice and water. The box in the photograph shows the same region of ice as the box in the CVV image. [After *Martin et al.*, 1992]

respectively [*Donelan and Pierson*, 1987, their Figures 4 and 5]. The thresholds increase slightly with increasing incident angle and decrease slightly with increasing ocean temperature.

Next we consider ocean surface backscatter in relation to wind speed and different radar system parameters including frequency, polarization, and incident angles. The ocean backscatter at all common SAR frequencies decreases quite sharply with increasing incidences between 20° and 50° (Figures 2.5 and 2.6), particularly in comparison with other natural surfaces [refer to *Ulaby et al.*, 1986]. Note that backscatter increases with increasing wind speed (Figure 2.5) and that vertical polarization returns are higher than horizontal polarization by several dB except at the steepest incident angles (0° to 20°) (Figure 2.6). The noise floor, termed the noise equivalent sigma naught (σ_{Neq}^0) of spaceborne C-band SAR instruments is usually less than -20 dB (for example, σ_{Neq}^0 for RADARSAT-1 is about -25 dB). Ocean returns which approach that level, during low winds and particularly at larger incident angles, may not produce adequate signal above the noise floor, thus limiting the quantitative usefulness of the measurement under those conditions. In general, the backscatter for cross polarization data (HV, VH but not shown here)

is usually uniformly 5 dB lower than HH polarization, often forcing the returns near to or below the σ_{Neq}^0 under most conditions. Considering Figure 2.6, also note that the difference between VV and HH increases with increasing incident angles with the largest difference at 5.5 GHz (C-band), and that the overall returns are highest at 5.5 GHz and lowest at 1.3 GHz (L-band).

An interesting example of Bragg scattering and radar frequency is shown in Figure 2.7. The three SAR images were simultaneously obtained over the St. Lawrence Island polynya in the Bering Sea on 22 March 1988, with the three-frequency NASA AIRSAR platform [Martin *et al.*, 1992]. A polynya is an open water region amidst sea ice, usually adjacent to land, where ice is continuously formed and transported away from the land by strong and continuous offshore winds, causing the newly formed ice to generally pile up against the thicker pack ice. The ice crystals are aligned into streaks that are approximately parallel to the wind direction, seen in the central region of each image, which are separated by open water.

Note in Figure 2.7 the complete reversal in contrast of the features in the three-frequency series. What is ice and what is ocean? A coincident hand-held image enabled the clear identification of ice and ocean through feature mapping. The backscatter from sea ice generally increases with increasing frequency while the opposite is true with ocean returns. The ice is bright at C-band and dark at P-band (500 MHz, 50-cm wavelength) over the new and young ice formed in the polynya; however the ocean is dark at C-band and bright at P-band. The L-band image is a confusing mixture of backscatter over the ice and ocean. How can the opposite trends in ocean backscatter be explained, where we might at least expect a strong ocean contribution at C-band? A nearby buoy (46017) record shows that the winds were consistently from the northeast at wind speeds greater than 8 m s^{-1} for several days before and up to the time of imaging. We speculate that steady winds blowing over fetch-limited open water may have resulted in a non-continuous distribution of wavelengths, with an apparently greater presence of Bragg waves at P-band than C-band.

One key parameter regarding radar and wind speed is that the wind speed varies depending on the orientation of the radar antenna look direction or azimuth angle with respect to wind direction. Winds coming towards (upwind) or away from (downwind) the antenna look direction have higher returns (several dB) than winds that are offset (crosswind) from the antenna direction (Figure 2.8). This is directly related to orientation and tilt of the Bragg waves with respect to the radar (see Section 2.2.C). Scatterometers make use of this pattern to derive absolute wind direction, through the use of multiple stick antennas or a rotating antenna with a fixed incident angle [see *Ulaby et al.*, 1986]. The fixed azimuth viewing of a SAR antenna means that wind direction cannot be resolved directly by backscatter alone, but requires other approaches such as feature detection, alternate data sources, and internal data characteristics (see discussion on wind speed in Section 2.3).

2.2.3 Interactions of Short and Long Waves

Modeling efforts have generally shown that Bragg scattering alone does not satisfactorily account for the measured intensity of microwave scattering returns or of SAR, with its additional complexity of its image formation process. As will be briefly described below and in detail in later chapters, comparable measured/modeled returns are approached when considering the interaction of Bragg waves with intermediate scale waves and underlying currents.

In addition to Bragg waves, sustained wind forcing produces longer waves—for this discussion longer than 50 m. Such waves may develop sufficient energy to propagate away from the influence of their generation region, becoming swell, to eventually dissipate on the beach as

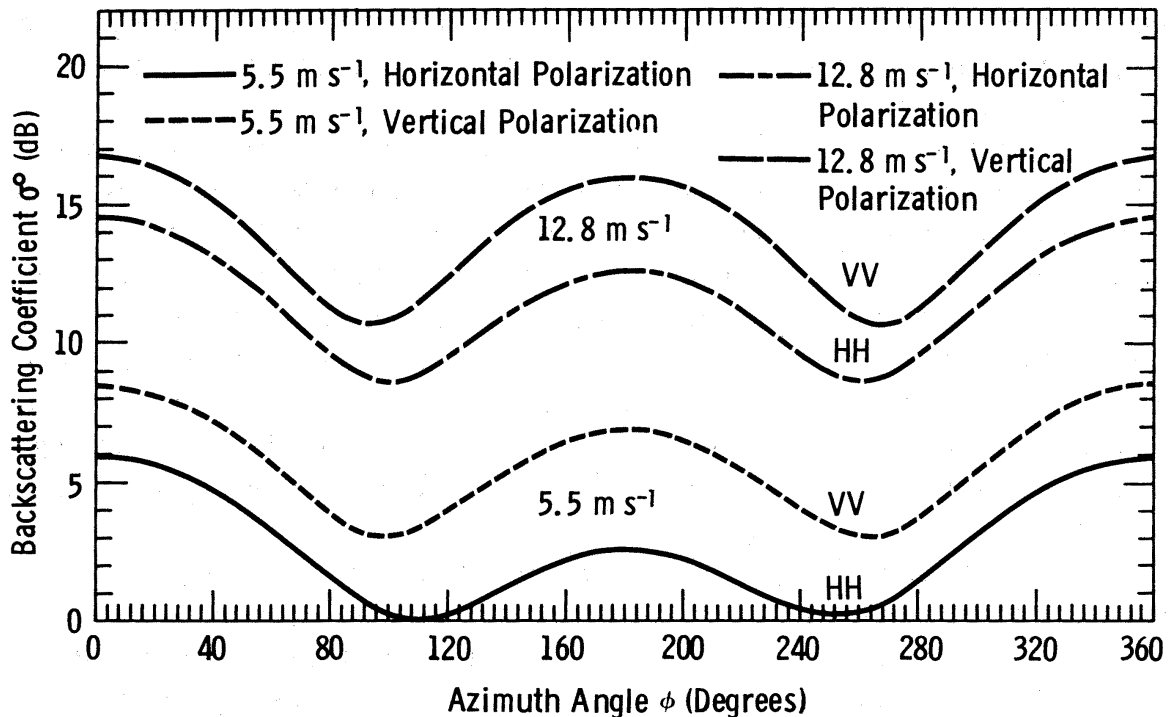


Figure 2.8. Azimuthal variation of the backscattering coefficient of the ocean surface at 14 GHz, where $F = 0^\circ$ and 180° corresponds to the upwind and downwind directions, respectively. [After *Ulaby et al.*, Vol. II, 1982, Figure 11.28]

surf or in the open ocean with wave-breaking or white-cap formation. In the open ocean, long waves have characteristic circular orbital or particle velocities which have sinusoidal directional components depending on position along the propagating wave (Figure 2.9). The slope, height, and orbital motion of the long waves interact with and redistribute the Bragg waves, producing an alternating radar intensity which is detectable on the fine resolution SAR imagery, often with extraordinary detail.

The interaction of short and long waves and how these interactions affect the radar scattering is referred to as the two-scale approximation. There are three primary mechanisms in which long waves modify Bragg waves to effect SAR imaging—the tilt, hydrodynamic and velocity bunching [for key seminal papers, see *Elachi and Brown*, 1977; *Alpers et al.*, 1981; *Alpers*, 1983a, 1983b; *Hasselmann et al.*, 1985]. It should be noted that when long waves enter shallow water, the orbital trajectories become elliptical, with the long axes in the horizontal direction which further effects the long wave-short wave interactions.

As the long waves propagate through the short wave field, two adjustments to the short waves are made that directly change the intensity and thus imaging of the radar returns. The first, tilt modulation, is when the varying slope of the long wave changes the local orientation or tilt of the short waves (Figure 2.10). These tilting waves act as reflecting mirrors or facets to the incoming radar waves, so that the return will vary as the facets change tilt along the longer propagating wave. The second adjustment, hydrodynamic modulation, takes place when the amplitudes of the short wave field are non-uniformly altered by the long wave in the following ways (Figure 2.10): the long wave orbital velocities (Figure 2.9) have different directions along the wave, which tends to pile up short waves in the convergence zones (crest) and spread them

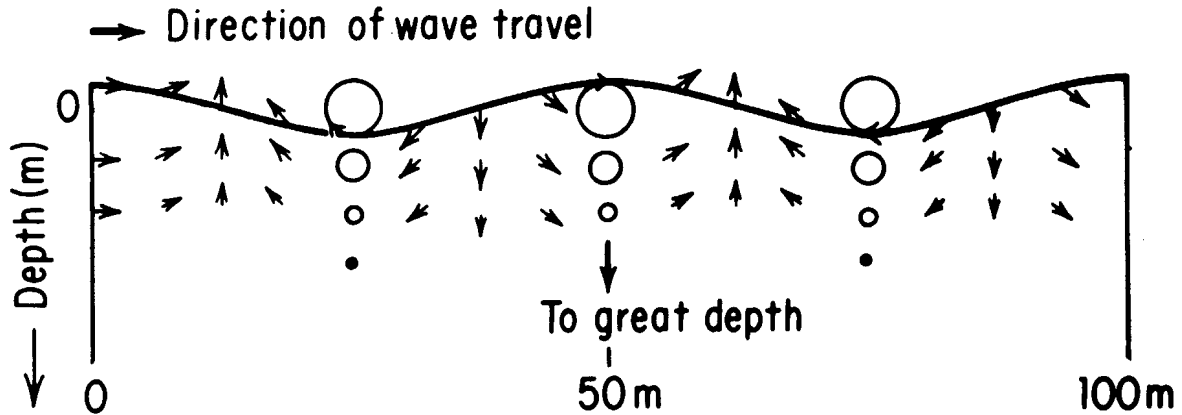


Figure 2.9. Instantaneous velocity vectors and orbital paths of fluid particles in a long wave in deepwater. Velocities become small at a depth equal to one-half the wavelength. [After Neumann and Pierson, 1966]

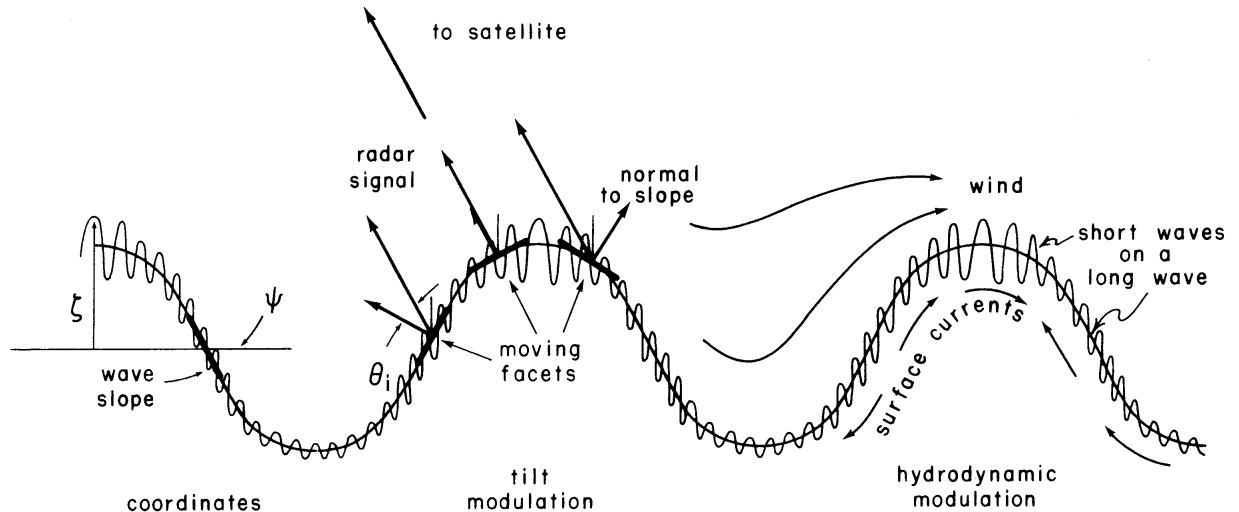


Figure 2.10. Illustration of tilt and hydrodynamic modulation. The longer waves change the local orientation or slope (tilt modulation) and distribution (hydrodynamic modulation) of the shorter wave fields. See text for further explanation. Symbols include local incident angle, θ , wavenumber spectrum, ψ , and sea surface elevation, ζ . [After Stewart, 1985, Figure 13.6]

out in the divergence zones (trough); and the airflow over the long waves is distorted, thereby preferentially forming short waves at the crest as compared to the trough. Both tilt and hydrodynamic modulations have the strongest effects on the radar returns when the long waves are propagating perpendicular to the radar platform direction (wave crests moving toward or away from the antenna, termed range-traveling). Both mechanisms are stronger at horizontal than vertical polarizations, with the relative importance of each varying with incident angle [e.g., Hasselmann *et al.*, 1985].

The third modulation, velocity bunching, is invoked when long surface waves are propagating in a direction parallel to the SAR platform direction or equivalently perpendicular to the radar antenna look direction (termed azimuth-traveling). The motion of the long waves alters

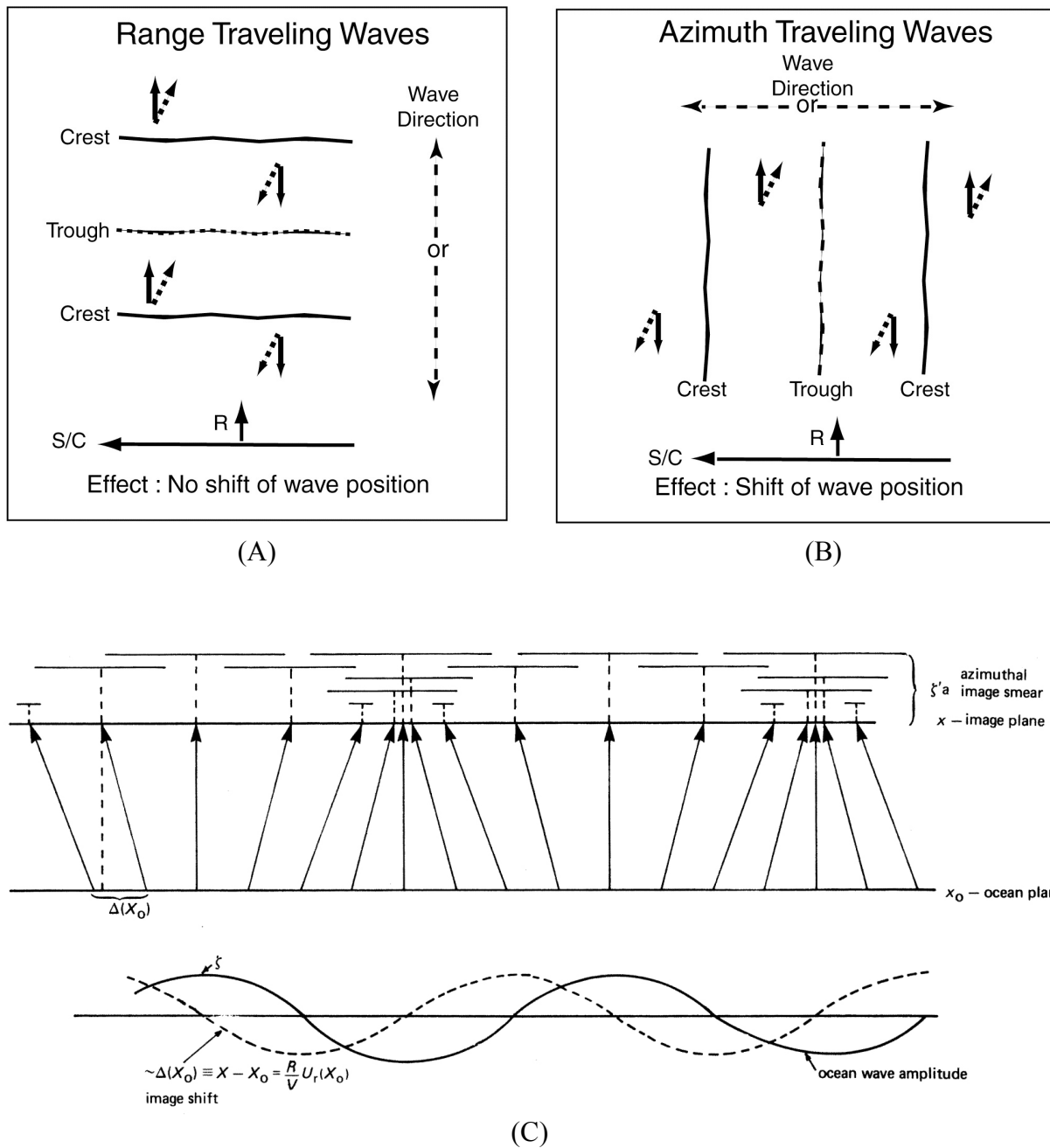


Figure 2.11. (a) and (b) Sketches of effect of Doppler offset related to spacecraft (S/C) flight direction, direction of radar imaging (R), and surface wave propagation direction (shown with a 180° ambiguity). The case for waves propagating (a) perpendicular or range traveling and (b) parallel or azimuth-traveling to spacecraft flight direction are shown. For waves, the heavy line indicates direction of velocity vectors and orbital path of wave particles within a deepwater wave (see Figure 2.9) while the associated dashed line represents the effective velocity vector as detected by the radar. (c) Illustration of velocity bunching modulation with azimuthal image shift and image smear associated with an ocean wave. The equally spaced facets on the ocean appear non-uniformly distributed on the SAR image plane and are smeared non-uniformly in the azimuth direction. Symbols include slant range, R , platform velocity, V , radial velocity component, u_r , and sea surface elevation, ζ . [After Alpers, 1983a]

the SAR imaging process, which nominally uses the Doppler signal over stationary targets to achieve its fine azimuth resolution. If a target has a velocity component, u , that is towards or away (radial) from the radar platform, the wave's orbital motion will produce an additional velocity or Doppler component which the radar interprets as a position shift in the azimuth direction. For range-traveling long waves, one point on a wave crest will be merely shifted forward or rearward to a similar relative position on the same wave crest and thus there is no apparent offset in the wave position (Figure 2.11a). For azimuth-traveling waves, the radial velocity component will have an apparent shift in the azimuth direction (Figure 2.11b). The periodic orbital motion of the long wave will produce an apparent increase (bunching) and decrease in the density of scatters, thereby making azimuth-traveling long waves detectable on the SAR image plane but shifted from their true position (Figure 2.11c).

However, the above conditions describe a uniform or coherent wave field, much different than the actual ocean surface. As long waves grow steeper, the radial velocity components increase, resulting in more random azimuth displacements. The azimuth shift, D , is estimated by considering the distance of the radar platform to the surface and the platform velocity, or

$$D = (R/V) u \quad (5)?$$

where R/V is the slant range-to-platform velocity ratio and u is the radial velocity component of a scatterer. With minimal displacements (less than a wavelength), azimuth-traveling waves are linearly mapped in the SAR imagery (Figure 2.11c). When the displacements are severe (greater than a wavelength), the mapping of waves on the imagery will be nonlinear and distorted [e.g., *Hasselmann et al.*, 1985].

As waves grow steeper, the radial velocity of azimuth-traveling waves increases, resulting in velocity displacements that the radar cannot track and smearing in the imagery. Termed the coherence time limitation, the smearing effectively reduces the azimuth resolution and thus limits the detectable ocean wavelengths. The minimum detectable wavelength, λ_{\min} , depends on the R/V ratio and significant wave height, H_s , as follows:

$$\lambda_{\min} = C_0 \frac{R}{V} \sqrt{H_s} \quad (6)?$$

where C_0 is a constant of order 1 with units ($\text{m}^{1/2} \text{s}^{-1}$). As the velocity of a spacecraft does not vary greatly with altitude, the orbital altitude becomes the controlling factor for R/V . Thus for a given sea state, λ_{\min} will be much larger at a nominal sun-synchronous earth orbit of 800 km than at a characteristic shuttle orbit altitude of about 230 km (see Chapter 5 for further details). As briefly mentioned in the introduction, the shuttle-based experiments of SIR-B and SIR-C/XSAR were particularly useful for surface wave studies and enabled considerable improvements in imaging theory and other corrections needed to unravel the non-linear aspects of wave imaging from satellites.

The two-scale approximation that includes the interaction of Bragg waves with long waves accounted for considerable understanding of sea surface scattering, but not under all wind and wave states and radar system configurations. For example, the scattering response from viewing at incident angles lower than 15° and higher than 50° required other mechanisms as did the differences between horizontal and vertical polarizations and differences in response over a wide range of frequencies and system parameters [e.g., *Valenzuela*, 1978; *Hasselmann et al.*, 1985]. Investigators have examined different components of the wave spectrum and found

additional wave-wave interactions, including in the intermediate scale range, that have helped to account for some of the earlier discrepancies [e.g., *Donelan and Pierson, 1987; Romeiser et al., 1997; Plant, 2002*]. So-called bound waves, which are short-capillary waves generated on steep and short gravity waves that move at the same speed as the steep wave (bound) rather than freely, have recently been found to improve measurement discrepancies at higher viewing angles [*Plant, 1997*] and over surface slicks [*Gade et al., 1998c*]. Similar considerations have improved understanding of wave-current interactions as discussed below.

2.2.4 Short Wave Interactions with Currents

The interaction of a surface wave field and variable currents produces an exchange of energy and momentum, which can significantly alter the surface wave field over several wavelength scales including but not exclusively at the Bragg scale. To first order, wave-current interactions can either increase or decrease the radar backscatter compared to the background returns. These interactions are sensitive to wind speed and direction, boundary layer stratification, sea surface temperature, and the presence of surface oil slicks. Characteristic examples are numerous [e.g., *Beal et al., 1981; Fu and Holt, 1982, 1983; Vesecky and Stewart, 1982; Johannessen et al., 1991, 1994, 1996; Nilsson and Tildesley, 1995; Lyzenga and Marmorino, 1998; DiGiacomo and Holt, 2001*]. On a larger scale, wave refraction can occur as swell passes through a large current or eddy [e.g., *Beal et al., 1983, 1986; Irvine and Tilley, 1988; Barnett et al., 1989; Liu et al., 1994*].

Wave-current interactions that are imaged by SAR fall into the following general categories: 1) an oscillating orbital particle motion within a current field may produce zones of converging or diverging flow, where short waves and/or surface slicks may, respectively, either accumulate or disperse; 2) horizontal shear flow at a current boundary may alter the short wave field, either through velocity variations or through wave refraction or reflection; and 3) a sharp sea surface temperature discontinuity may alter the stability of the boundary layer. Often, all of these general categories may be contributing to any single detected feature. Sharp salinity gradients including oceanic fronts, freshwater river plumes, and melting ice may also be detectable on SAR imagery [e.g., *Fu and Holt, 1982*], but these returns are complicated by sea surface temperature gradients, winds, oils, and sediments, such that sorting out the influence of the salinity gradient itself becomes difficult. The radar returns from wave-current interactions will vary with several radar system parameters, including frequency, polarization, and viewing geometry in relation to current direction and wind speed and direction. In terms of frequency, wave-current imaging models generally are able to account for the L-band returns, but difficulty has been encountered for X- and C-bands as the models have underestimated the measured intensity of the radar returns. The end result is that while there is increased understanding of SAR imaging of wave-current interactions, the modeling efforts to date tend to have constrained the problem rather than to have been conclusive.

Examples of convergent and divergent flow include internal waves, surface currents ranging from alterations of currents due to bathymetry up to western boundary currents, and mesoscale to small-scale eddies. In one example, *Lyzenga [1998]* proposed that at X- and C-bands, short Bragg waves interact with intermediate scale waves of about 1 m and both scales interact with large-scale currents associated with internal waves and ocean fronts to produce amplification of short wave steepness and thus enhanced radar returns. *Thompson [1988]* proposed similar interactions for L- and X-band data. For bathymetry, the current speed varies over the varying bottom profiles, also producing convergent/divergent zones which

enhances/decreases the steepness of intermediate waves and thus related increase/decrease in radar brightness [e.g., *Romeiser and Alpers*, 1997]. Often internal waves, currents, and small-scale eddies are also associated with a lower return resulting from surfactants that accumulate in well-organized convergent zones and effectively suppress Bragg waves. Atmospheric boundary layer waves (lee waves and roll vortices, as discussed in Section 2.3.2) also appear on radar imagery due to convergent/divergent flow patterns, as the flow fields within the boundary layer waves either accumulate or disperse the short waves on the ocean surface.

A shear or current gradient within a meandering current may modify the short wave spectrum, causing either an enhanced or suppressed radar return compared to the background [*Johannessen et al.*, 1996; *Lyzenga*, 1998; *Lyzenga and Marmorino*, 1998] (Figure 2.1). The wave spectrum and the angle of the wave field as it encounters the current gradient are key to the ensuing changes in the wave characteristics, resulting in reflection or refraction or even transmission. Another factor is the viewing geometry of the SAR platform with respect to the current front.

A fairly sharp sea surface temperature boundary or front (about 2°C or greater) between adjacent water masses, for example shelf and slope water, offshore jets, upwelling zones, and eddies, may alter the radar return in at least two ways [e.g., *Lyzenga*, 1991] (Figure 2.1). One case is that the boundary layer over cold water has increased stability as compared to adjacent warmer water, which results in decreased local wind drag and smoother surface roughness. The level of change in backscatter is related to the temperature gradient between water masses, and wind speed and direction. In the other case, lower surface temperatures also lower viscosity and effectively suppresses capillary waves [*Kinsman*, 1984]. This effect is most important at higher frequencies such as X- and C-band [*Donelan and Pierson*, 1987], but is generally less important than the impact of boundary layer stability across a sharp sea surface temperature gradient [e.g., *Clemente-Colòn and Yan*, 1999].

2.2.5 Oil Slicks on the Sea Surface

Oil on the sea surface is effectively seen on SAR ocean images as zones of reduced backscatter. The viscoelastic property of oil slicks effectively dampens the short-wave field by both suppression of wave growth and increase in wave dissipation, through an increase in surface tension and a reduction in wind friction. Oil slicks may be confused on SAR imagery with areas of low wind and other low-backscatter features such as cold and freshwater masses. Distinguishing oil from low wind, especially in zones of recurring oil seeps, is usually done through repeat imaging and knowledge of wind history to account for varying shapes as the wind disperses oil in different directions. Oil may also become distributed within currents, eddies, and internal waves in characteristic ways, often providing a key mechanism for detection of the features.

Surface slicks in the ocean are composed of two major forms of oil. Biogenic oils, often called surface active agents or surfactants and/or natural films, occur in a thin monolayer and are highly viscoelastic oils that are a by-product of ocean plant and animal growth [*Bock and Frew*, 1993; *Liss and Duce*, 1997]. Surfactants readily accumulate in convergent zones by internal waves and current/eddy fields, but are mixed into the upper ocean and rapidly disperse and disappear under windy conditions. The other major form is mineral oil, which comes from multiple sources: natural oil seeps [*Hornafius et al.*, 1999], spills from ships and drilling platforms, and discharge from urban storm-water run-off. Mineral oils spread into thin layers

through gravity and surface tension, are volatile and evaporate and weather over time, and are dispersed by wind, waves, and currents [Fingas and Brown, 1997].

To first order, biogenic and mineral oils have typical thickness layers on the order of 10^{-7} m and 10^{-6} m, respectively. Combined with low dielectric constants between 2 and 3 [C.E. Brown, personal communication], both forms of oil are essentially transparent to radar at common SAR frequencies (1 to 10 GHz) and associated penetration depths (10^{-4} to 10^{-3} m). Thus, SAR images the presence of surface slicks primarily because of the ability of both forms of oil to smooth the sea surface and is not sensitive to thickness.

2.3 Characteristics of Ocean Features on SAR Imagery – A Guide

Examining imagery of the ocean surface from radar imagery is either fascinatingly complex or as uneventful and dull as watching paint dry. The detailed view of the ocean surface produced on SAR imagery is unique and not very well understood. This section will seek to characterize the wide range of ocean features that commonly appear on SAR imagery and will provide representative examples at enlarged scales to highlight detailed imaging properties, often accompanied by a graphic of the surface interaction and/or resulting signature. A brief description of the primary uses of the imagery is also included. Table 2.1 summarizes the groups of features by scales, measurements derived from the features, imaging mechanisms (referring to Section 2.2), range of wind speed over which the features may be observed, and other key characteristics and considerations. Using this section as a guide, the reader should get a good sense for interpreting SAR ocean imagery and what quantitative information can be derived about the upper ocean and air-sea interactions.

2.3.1 Ocean Features

2.3.1.1 Surface Waves. SAR imagery of surface waves have been extensively analyzed and utilized in many different applications. The fine resolution of SAR (around 25 m) provides the most consistent two-dimensional imaging of ocean waves of any spaceborne remote sensor. The directional ocean wave spectra derived from SAR imagery has provided information on the spatial evolution of regional and global wave fields [e.g., Beal *et al.*, 1983, 1986], wave fields generated by storms and hurricanes [e.g., Gonzalez *et al.*, 1987; Holt *et al.*, 1998], and wave refraction through currents and eddies [e.g., Irvine and Tilley, 1988; Liu *et al.*, 1994]. SAR wave imagery has also been used to improve wave prediction through assimilation of SAR wave spectra into wave forecast models [e.g., Beal, 1991] and for deriving information on sea ice through wave propagation into the ice cover (see Chapter 5 for additional references). Surface waves interact with SAR through the three primary mechanisms discussed in Section 2.2.B: tilt, hydrodynamic, and velocity bunching transfer functions. Velocity bunching is of particular importance as it accounts for the potential (and probable with spaceborne SAR) severe non-linear distortions in the directional wave spectra for azimuth-traveling waves. Usually SAR-derived wave propagation direction is provided with a 180° ambiguity, which can be resolved from independent weather and wave information. Recently, an approach has been developed, called the inter-look cross spectra, which derives absolute direction from the data itself by examining the imaginary component of individual looks in the SAR image formation process [Engen and Johnsen, 1995; Dowd *et al.*, 2001]. This approach has been incorporated in the ENVISAT ASAR surface wave products.

Surface waves are seen as fine-scale periodic patterns where the wave crest is brighter

Table 2.1. Characteristics of Ocean Features on SAR imagery (Part I)

OCEAN FEATURES					
Feature	Scale	Derived Measurement	Imaging Mechanism	Range of Wind Speed m s⁻¹	Characteristics and Considerations
Surface Waves	100-600 m wavelength	Wavelength Propagation direction Wave height	Tilt Hydrodynamic Velocity Bunching	3-40	Azimuth-traveling waves may be nonlinear without correction. Other limiting factors include wavelength, wave height and fetch.
Internal Waves	0.3-3 km wavelength	Wavelength Direction Amplitude Mixed layer depth	Convergence/Divergence Surfactants	2-10	Curvilinear packets with multiple waves, decreasing wavelength from front to back. Sensitive to wind conditions, wave crest orientation to platform.
Internal Tides	10-20 km	Wavelength Direction	Interaction of centimeter Waves/Currents/Surfactants	3-7	
Currents and Fronts	1-100 km	Location Shear Strain Velocity	Shear/Convergence Convergence Wind stress Surfactants	3-10 3-10 3-10 3-7	Sensitive to wind conditions. Often multiple mechanisms present simultaneously.
Eddies	1-200 km diameter	Location and source Diameter Velocity Shear Strain	Shear/Convergence Wind Stress Surfactants	3-10 3-10 3-7	Sensitive to wind conditions. Often multiple mechanisms present simultaneously.
Shallow Water Bathymetry	5-50 m depth	Location/change detection Current velocity Depth	Convergence	3-12	Sensitive to wind, current properties, depth.

Table 2.1. Characteristics of Ocean Features on SAR imagery (Part II)

AIR-SEA INTERACTIONS					
Feature	Scale	Derived Measurement	Imaging Mechanism	Range of Wind Speed $m s^{-1}$	Characteristics and Considerations
Surface Winds	>1 km grid	Wind speed Wind direction	Wind stress Indirectly via windrows, models, other sensors	3-25	For mesoscale, coastal variability. Requires good calibration.
Roll Vortices	1-5 km wavelength	Boundary Layer: Stratification	Wind stress	3-15	Long axis/crests parallel to wind direction.
Gravity Waves	2-10 km wavelength	Height Turbulence spectrum Drag coefficient	Wind stress	3-15	Long axis/crests perpendicular to wind direction, often associated with topography
Rain Cells	2-40 km diameter	Rain rate	Wind stress Rain damping	3-15	Appearance sensitive to frequency, rain rate, wind speed
OIL SLICKS					
Feature	Scale	Derived Measurement	Imaging Mechanism	Range of Wind Speed $m s^{-1}$	Characteristics and Considerations
Biogenic Surfactants	>100 m^2 area	Areal extent	Convergence	2-8	Both forms have signatures similar to low wind, cold thermal water masses etc.
Mineral Oils			Seeps Ship discharge Run-off	3-15	Wind speed, combination of L- and C-/X-bands may enable discrimination of each form.

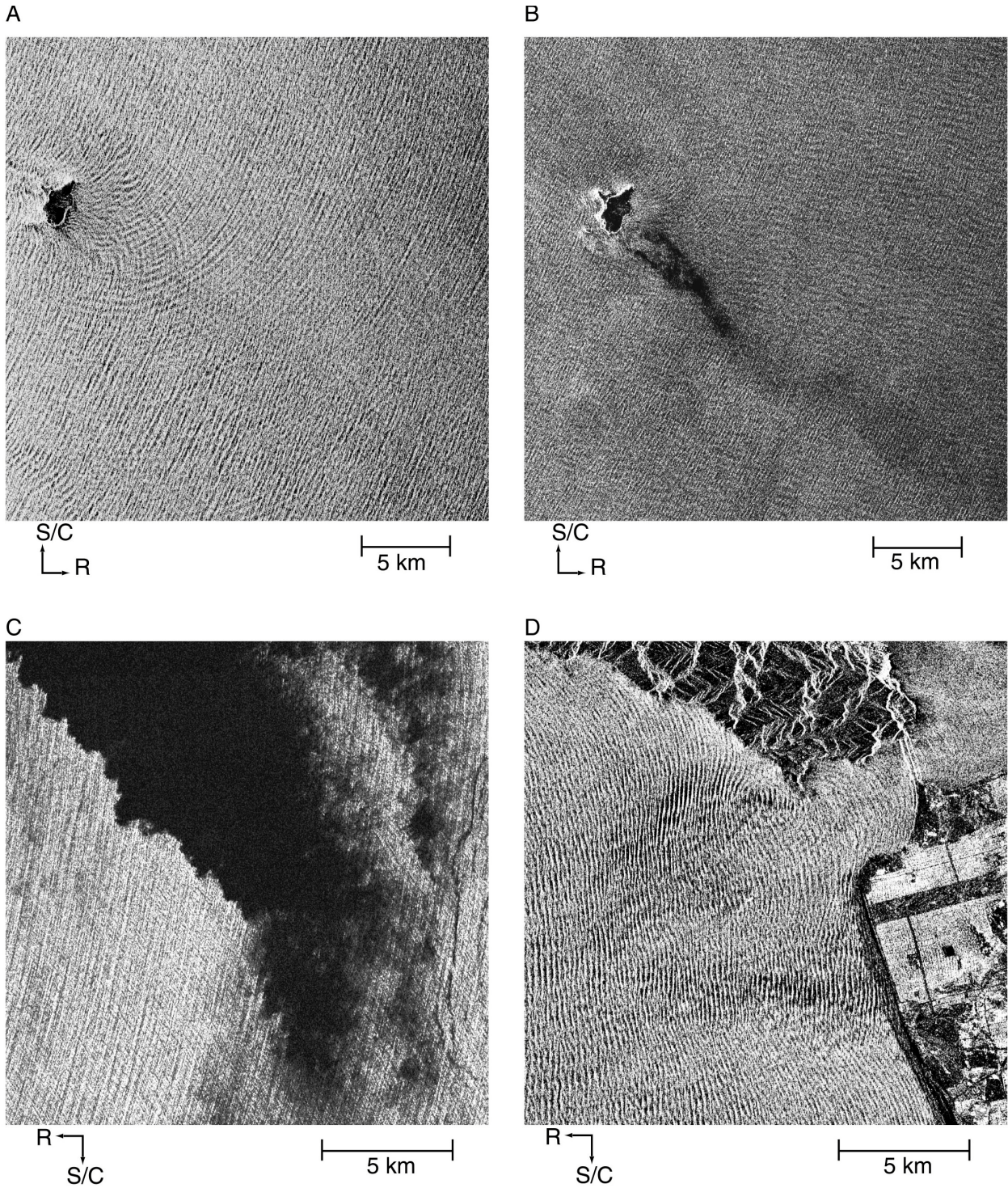


Figure 2.12. RADARSAT-1 (C-band, HH) SAR imaging of surface waves. (a) Range-traveling waves refracting around Santa Barbara Island (25 November 1998), (b) Dominant azimuth-traveling waves (north-south component) and finer-wavelength range-traveling (west-east component) waves near Santa Barbara Island (9 November 2001), (c) Surface waves under low wind conditions near San Clemente Island (2 December 1998), (d) Complicated wave patterns near San Francisco Bay including refraction into bay entrance (22 November 2001). RADARSAT Images ©CSA1998, 2001

and the wave trough darker than the overall returns from the mean wave field. The examples in Figure 2.12 show both range- and azimuth-traveling waves, the appearance of waves during low winds, and wave refraction past a headland. Deep-water swell is principally detected, as wind waves are either subject to non-linearities, are too short, or do not have sufficient directional energy to be isolated from the radar system noise. The scale of detected ocean waves falls between 100 and 600 m, where the minimum detectable wavelength is limited by azimuth smearing. Surface waves have been imaged in hurricanes with wind speeds over 40 m s^{-1} .

2.3.1.2 Internal waves. One of the unexpected results from SEASAT, confirmed extensively with the two ERS missions and RADARSAT-1, has been the nearly ubiquitous imaging of internal waves (Figure 2.13). Internal waves contribute to the energetics of the upper ocean and enhance mixing and nutrient availability. Internal waves seen on SAR imagery generally form along the stratified seasonal thermocline just below the upper ocean mixed layer, generated by tidal forcing over abrupt topographic features [e.g., *Apel*, 1987]. The subsurface waves are manifested on the ocean surface through the interaction of the current field of the internal wave with wind-driven surface waves. This interaction has been modeled based on the strain rate, which is the horizontal surface current gradient [e.g., *Liu*, 1988; *Lyzenga and Bennett*, 1988]. Internal waves appear as packets or groups of waves, characterized by curvilinear wave crests (bent by refraction) and by decreasing wavelengths from front to back of each packet (indicating that nonlinear wave dispersion is in effect and also indicating propagation direction). Adjacent packets have likely been generated during successive tidal cycles, so that wave group speed can be estimated by the distance between wave groups divided by tidal period [e.g., *Fu and Holt*, 1984].

The surface expressions of internal waves are alternating bands of rough and smooth water, which are particularly sensitive to wind. The most common appearance is a bright enhanced wave band, often with an adjacent dark band (Figure 2.13). The bright band is associated with the convergence zone, as determined by the orbital particle motion within the internal wave. In this case, short surface waves are piled up in the most turbulent part of the convergence zone. The dark band is often composed of surfactants that accumulate in the less turbulent part or divergence zone of the propagating wave and effectively dampen the short waves. Less often, internal waves may also be seen composed of only dark bands with no associated bright bands. Two detailed studies indicate that within a series of wave packets, each of the three various appearances may occur [*da Silva et al.*, 1998, 2000]. This varying appearance is due to sensitivity to wind speed (where higher winds may disperse the surfactants while the brighter convergence zone is still present) and to orientation of the wave groups to the radar platform and wind direction. For higher amplitude nonlinear solitons, it has been found that the nominal depression waves propagating shoreward (bright zone followed by dark zone on radar) may become elevation waves when the bottom layer becomes thinner than the mixed layer [*Liu et al.*, 1998; *Zheng et al.*, 2001]. This results in a reverse sense of the orbital particle motion and a subsequent reversal of the radar pattern within each packet where the dark band now appears ahead of the bright band for each wave.

In general, SAR imagery detects internal waves with wavelengths between 0.3 and 3 km, although one study revealed internal tidal waves with wavelengths between 10 and 20 km [*Ermakov et al.*, 1998]. Internal waves have been detected at wind speeds between 2 and 10 m s^{-1} . SAR studies have been done over broad continental shelves, irregular and narrow shelves, and for waves generated over sills, through straits, canyons and sea mounts. Studies have

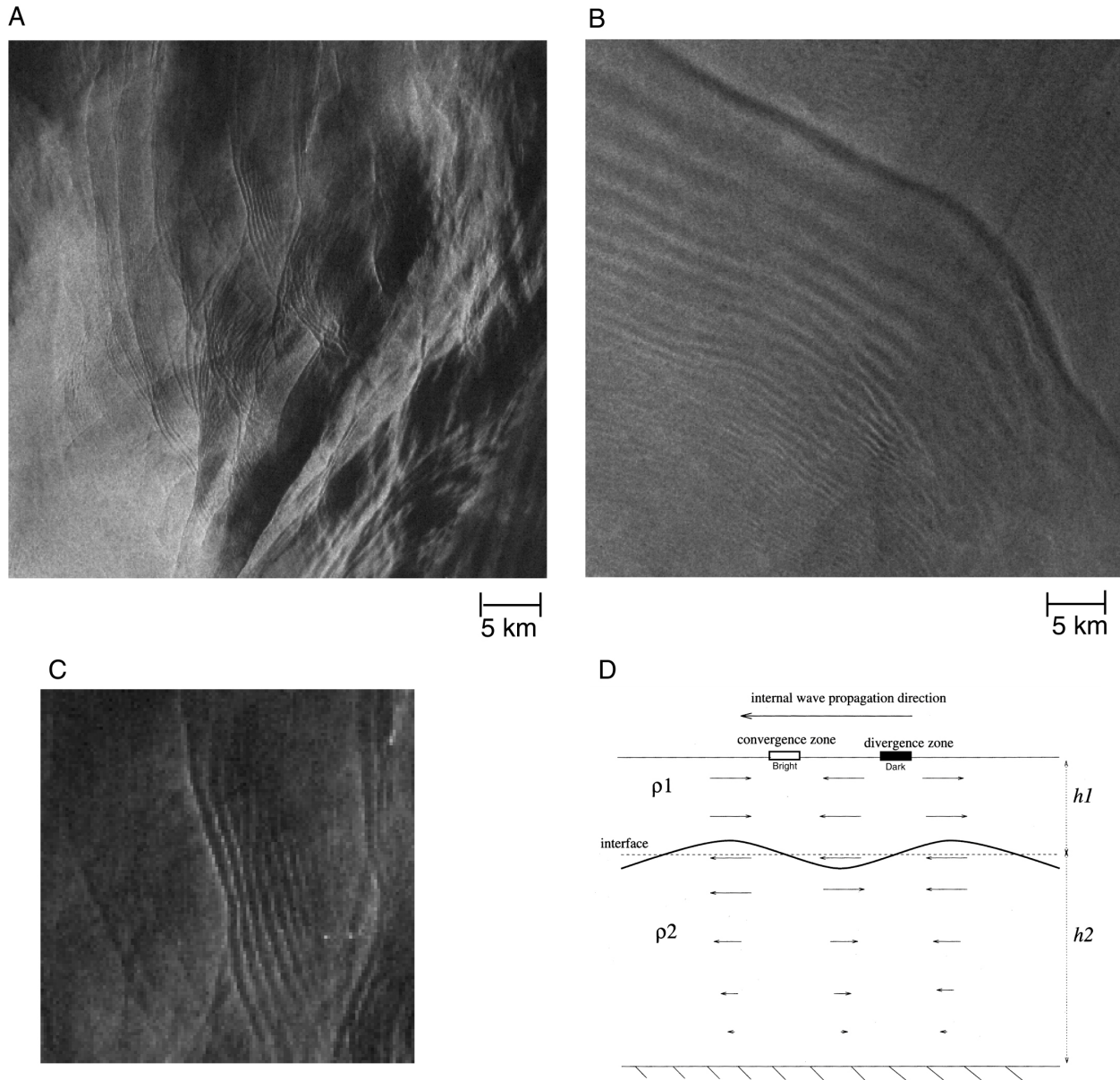


Figure 2.13. SEASAT (L-Band, HH) SAR imaging of internal waves. (a) Comparatively fine-scale internal wave packets along the shelf break east of Cape Canaveral, Florida adjacent to the Gulf Stream (25 July 1978), (b) Larger-scale internal wave packet within the Gulf of California (29 September 1978), (c) Enlargement of one packet from (a) to highlight bands of enhanced backscatter at front of each wave followed by adjacent band of decreased backscatter, relative to surrounding surface backscatter; (d) Sketch illustrating relative direction of particle motion within the internal wave as it propagates along the seasonal thermocline and the subsequent formation of convergent and divergent zones [After Johannessen *et al.*, 1994]. The small gravity waves tend to be piled together (converge) or spread apart (diverge) in the two zones, with direct consequences on the radar backscatter.

examined the dissipation of tidal energy to internal waves [Fu and Holt, 1984], the estimation of internal wave amplitude based on surface scattering [Gasparovic *et al.*, 1988; Zheng *et al.*, 2001], and mixed layer depth and velocity based on comparisons of SAR-derived and modeled group velocity [Porter and Thompson, 1999; Liu *et al.*, 1998; Li *et al.*, 2000]. An internal wave climatology off Norway was developed based on over 2600 images [Dokken *et al.*, 2001].

2.3.1.3 Currents, Fronts, and Eddies. The capability of SAR to improve our knowledge of the ocean's mesoscale circulation, particularly in the coastal zones, may turn out to be its most important contribution to ocean science. Mesoscale current features are seen because of short wave-current interactions along zones of convergence and shear boundaries (Figure 2.14), a change in boundary layer stability and wind stress across a sharp temperature gradient, and accumulation of surfactants within eddies and convergence zones which suppress short waves and serve as current tracers (Figure 2.15). However, there is much remaining to learn as the SAR signatures of currents, fronts, and a wide size range of eddies have proven to be highly complex. Reliable derivation of properties such as velocity, strain, and shear, either through modeling or validation with experimental measurements, has proven elusive. It is even difficult to provide conclusive examples of images with isolated imaging mechanisms. Rather, one must start with the assumption that the signature of any particular feature has several simultaneous contributing mechanisms.

The types of features that have been detected and analyzed with SAR imagery include the following: 1) currents of various scales including western boundary currents, such as the Gulf Stream [Lyzenga and Marmorino, 1998; Marmorino et al., 1999], East Australia [Nilsson and Tildesley, 1995], and more recently the Brazil-Malvinas Confluence [Gagliardini et al., 2001], as well as smaller coastal currents [Johannessen et al., 1991, 1996]; 2) eddies ranging in size from submesoscale spiral eddies [Johannessen et al., 1996; Munk et al., 2000; DiGiacomo and Holt, 2001] (Figure 2.15) up to those shed by the Gulf Stream (Figure 2.14) [Lichy et al., 1981]; and 3) thermal and current fronts, although these may also overlap with currents and eddies. Numerous studies have combined both SAR and sea surface temperature (SST) imagery, often finding a high correlation of thermal fronts with SAR signatures (Figure 2.15). Often, however, there may be reduced thermal contrast in the summer due to solar heating. This suggests that SAR can compliment SST detection of mesoscale variability during those periods [e.g. Fu and Holt, 1983; Johannessen et al., 1996; Martinez-Diaz-De-Leon et al., 1999; Gagliardini et al., 2001].

Several studies have compared SAR imagery to numerical simulation of the SAR returns, to help isolate the contribution from environmental conditions and to derive estimates of strain rates, shear, and velocity [e.g., Johannessen et al., 1996; Ufermann and Romeiser, 1997; Chubb et al., 1999]. In one case, convergence and cyclonic vorticity were estimated by slick motion [Lyzenga and Marmorino, 1998]. The size and seasonal distribution of small eddies were mapped in a coastal region [DiGiacomo and Holt, 2001]. Zones of coastal upwelling have been identified through reduction of wind stress [Clemente-Colòn and Yan, 1999]. The refraction of longer waves through current fields has been examined as an approach to derive current velocity within boundary currents and mesoscale eddies [e.g., Beal et al., 1986; Irvine and Tilley, 1988; Barnett et al., 1989; Liu et al., 1994; Johannessen et al., 1996]. In nearly all these studies, the surface expressions are wind-speed dependent. Winds above 6 to 7 m s⁻¹ disperse surfactants, removing that mechanism for detectability [Johannessen et al., 1996; DiGiacomo and Holt, 2001]. Shear/convergence enhanced lines appear to be detectable up to about 10 to 12 m s⁻¹, after which they are not detectable from the surrounding ocean background returns [e.g., Johannessen et al., 1996].

2.3.1.4 Bathymetry. We briefly examine the SAR signatures over shallow bathymetry as they are similar to those of internal waves. Tidal currents flowing over undulating shallow bottom features produce patterns on SAR that are somewhat self-similar but are perhaps best characterized as site-specific (Figure 2.16). The alternating sawtooth signatures are dependent

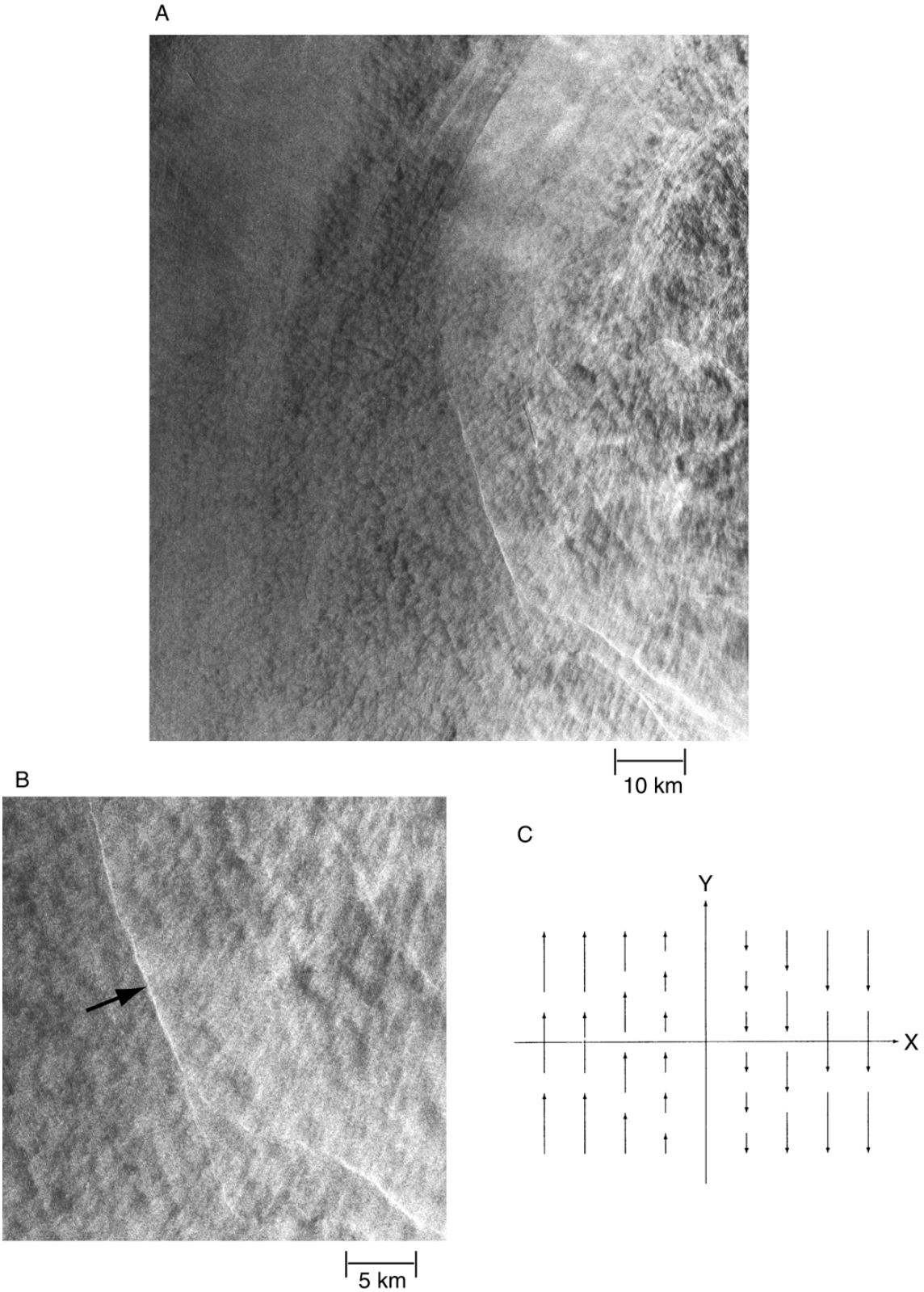


Figure 2.14. Current shear associated with a Gulf Stream warm ring (a) imaged by SEASAT (L-band, HH), on 21 September 1978. (b) Enlargement from (a) of current shear (arrow) which appears as a narrow bright line (c) with an illustrative sketch [After Lyzenga, 1991].

SAR Imaging of the Ocean Surface

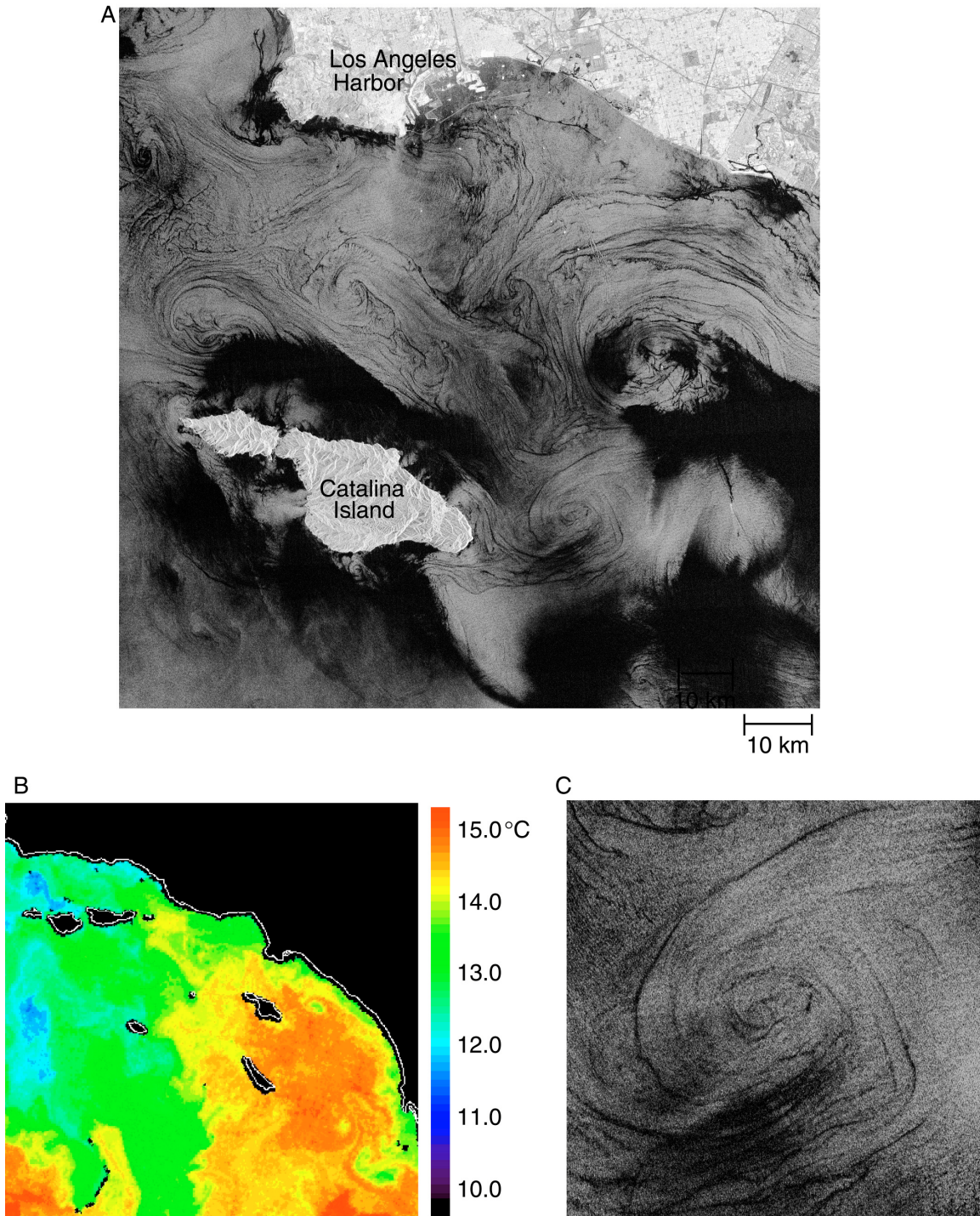


Figure 2.15. Small-scale eddies in the Catalina Channel off Southern California as seen from (a) RADARSAT-1 (C-band, HH) (26 December 1998) and (b) associated sea surface temperature image from AVHRR (25 December 1998). In the SAR image, the eddies are largely detectable by the series of dark spirals associated with biogenic oils. (c) An enlargement of the eddy in (a) located east of the east end of Catalina, which shows little indication of a sea surface temperature signature in (b) while the adjacent eddy to the northeast (a) has a strong temperature signature. We speculate that the sea surface temperature expressions or lack thereof of the eddies, may be related to the eddies' scale, period of life-cycle, generation mechanism, or some combination of all of these. RADARSAT Images ©CSA 1998

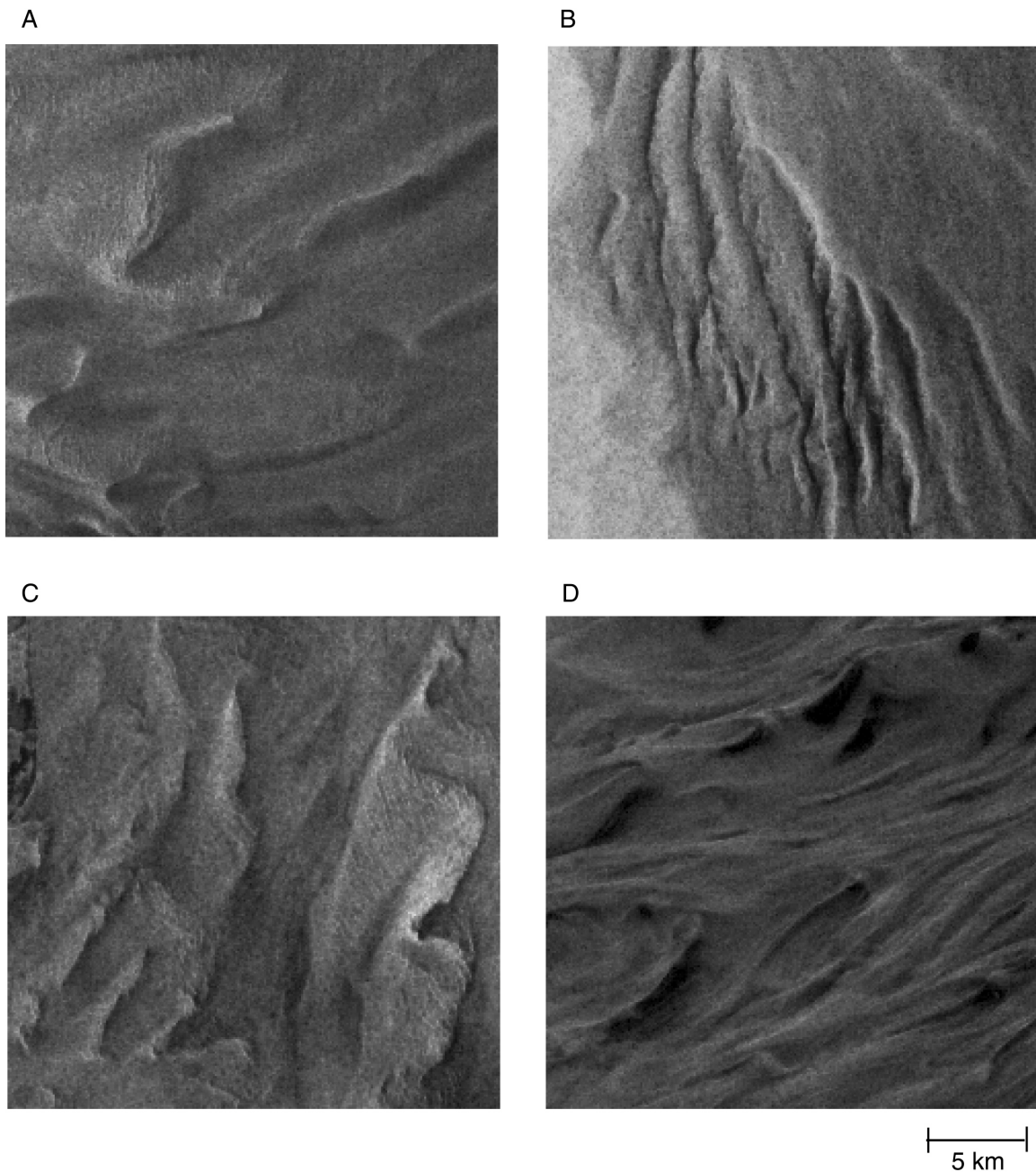


Figure 2.16. Bathymetric expressions from SEASAT (L-Band, HH) SAR. (a) English Channel, 19 August 1978, (b) Tongue of the Ocean, Bahama Bank, 3 October 1978, (c) Nantucket Shoals, 27 August 1978, (d) Kuskokim River, Alaska, 13 July 1978. [After *Fu and Holt*, 1982]

on current flow direction in relation to the bottom feature height and whether the current is increasing or decreasing [*Alpers and Hennings*, 1984; *Romeiser and Alpers*, 1997; *Romeiser et al.*, 1997; *Vogelzang*, 1997; *Vogelzang et al.*, 1997]. Bathymetric studies have focused on the English Channel, Nantucket Shoals, and entrances to bays and rivers. The studies have attempted to use the SAR patterns to determine current velocity and the position and depth change of bottom features over time.

2.3.2 Air-sea Interactions

Starting with SEASAT, it became clear that the spaceborne SAR ocean imagery was revealing detailed imprints of atmospheric phenomena which could not be attributed to ocean features [Beal *et al.*, 1981; Fu and Holt, 1982]. These phenomena ranged from gusty, patchy low winds to windrows indicative of strong winds and from rain cells to hurricanes. The C-band SAR data from the ERS platforms and RADARSAT-1 were found to be more sensitive to air-sea interactions than SEASAT's L-band SAR. This has sparked the interest of atmospheric scientists, and has resulted in extensive studies over the last decade that have expanded the list and quantification of identifiable atmospheric features seen on SAR ocean imagery. In general, the features have characteristic appearances and length scales to enable identification. This list of features covers a wide range of scales from turbulence (order 1 to 2 hundreds of meters) to mesoscale (order few hundred kilometers) [e.g., Mourad, 1996; Mourad *et al.*, 2000; Young, 2000]. In addition to windrows and rain cells, the list now includes atmospheric lee waves, fronts, convection within storms, and, in coastal areas, polar lows, vortex streets, and gap and katabatic winds. Generally, the identification, scales, and varying wind speed estimations of these features provide valuable information for understanding the properties of the boundary layer such as height and dynamics at scales that are otherwise difficult to measure.

2.3.2.1 Surface winds. Throughout the discussion so far, it is clear that the wind field has a critical effect on ocean imaging with SAR. As discussed previously, radar backscatter increases with increasing wind speed and is anisotropic in relation to relative wind direction (Figure 2.8). Spaceborne scatterometers have antenna configurations designed specifically to isolate direction with considerable certainty. The remaining combination of very good calibration (accuracy on the order of 0.2 to 0.4 dB) and wide swaths (500 to 1600 km) have enabled the historical and current scatterometers to produce global measurements of wind speed and direction, albeit at coarse resolutions on the order of 25 to 50 km. Scatterometry measurements have become so reliable that they are being directly assimilated into global weather analysis and forecasting models.

Because of its fine resolution, SAR has been shown to provide accurate wind speed (order $\pm 2 \text{ m s}^{-1}$ over speeds of 3 to 25 m s^{-1}) and direction (order $\pm 20^\circ$ to 30°) at kilometer scales (see Chapter 13), thereby providing sampling of regions with highly variable winds which cannot be effectively sampled by scatterometers. These regions include coastal zones and around islands, and where high wind gradients might be present, including temperature and wind fronts, large storms, and rain cells [e.g., Beal and Pichel, 2000]. As spaceborne SAR is limited to one viewing direction per image pass, different approaches to resolve wind direction have been examined. These include the use of various wind features on the SAR imagery, near coincident scatterometer measurements, wind forecasts, and in-situ observations. In turn, accurate wind direction estimates further improve the wind speed errors.

Using SEASAT SAR data, Gerling [1986] used the appearance of windrows or roll vortices (defined in next section) as a proxy for direction, since these boundary layer features are aligned with the mean wind direction. The L-band SAR data, which had only relative and not absolute radiometric calibration, qualitatively compared favorably with results from the SEASAT scatterometer. Following SEASAT, both ERS missions provided a unique instrument configuration that enabled considerable advances in SAR wind speed measurements. The ERS SAR and scatterometer used the same C-band VV instrument electronics package, called the advanced microwave instrument (AMI), with separate antennas. Eventually a high quality wind

speed algorithm was developed over 18° to 59° incident angles called CMOD4 [Stoffelen and Anderson, 1997]. Using this same algorithm, several studies examined the use of the comparatively narrow-swath ERS SAR for wind speed [e.g., Korsbakken et al., 1998; Lehner et al., 1998; Fetterer et al., 1998] and specific techniques for utilizing windrow orientation for direction [Wackerman et al., 1996]. Most of these studies also identified specific environmental and ocean conditions which contributed to variability as well as measurement error including relative wind direction, fetch, presence or absence of windrows, temperature and atmospheric fronts, proximity to land, and high or low winds.

The wide-swath capabilities of RADARSAT-1 have been recently examined including extensive demonstration experiments designed to specifically develop such measurements for operational weather forecasting [Pichel and Clemente-Colòn, 2000]. This effort was first focused on deriving accurate polarization ratios needed to convert the ERS (CVV) CMOD4 wind retrieval algorithm to RADARSAT-1's HH polarization [e.g., Thompson and Beal, 2000; Vachon and Dobson, 2000; Wackerman et al., 2002]. The differences of about $\pm 2 \text{ m s}^{-1}$ between SAR wind speeds using direction derived from buoys and models [Monaldo et al., 2001] were further reduced to about $\pm 1.5 \text{ m s}^{-1}$ when QuikSCAT wind directions were used [Thompson et al., 2001]. A recent paper derived a wind speed model from the JERS-1 L-band over a limited range of incidence angles [Shimada et al., 2003]. As mentioned previously L-band is not as sensitive to wind speed as higher frequencies, but in its favor are that the returns will saturate at higher winds speeds and Bragg scattering has a slightly lower threshold wind speed as compared to C-band.

2.3.2.2. Windrows or roll vortices. Windrows or roll vortices are organized counter-rotating secondary circulations, embedded in the mean flow, that result from instabilities in the convective marine boundary layer [Brown, 1980]. The long axes of the windrows are approximately parallel to the mean surface wind direction and the wavelength spacing is related to the thickness of the planetary boundary layer. Roll vortices are seen on SAR imagery as adjacent periodic bands of bright and dark radar returns with wavelengths between 1 and 5 km which may broaden up to 10 to 15 km [e.g. Fu and Holt, 1982; Mourad and Walter, 1996; Brown, 2000] (Figure 2.17). The alternating SAR returns are directly related to fluctuations in along-wind velocity within the near-surface convergent or divergence regions [Alpers and Brümmer, 1994; Vandemark et al., 2001] (Figure 2.17c). As mentioned previously, Gerling [1986] used the orientation of the roll vortices to specify wind direction with SEASAT SAR. Later results using C-band imagery determined the overall biased directional offset to be 10 to 15° clockwise in the northern hemisphere [Wackerman et al., 1996; Worthington, 2001]. Levy [2001] developed a regional climatology of roll vortices, finding the frequency of occurrence often exceeding 40%.

2.3.2.3. Atmospheric gravity waves. Atmospheric gravity waves observed in SAR images form by a disturbance in the stable, stratified lower atmosphere, often appearing downstream of topographic features or the sea ice edge [Vachon et al., 1994; Alpers and Stilke, 1996; Zheng et al., 1998; Chunchuzov et al., 2000; Worthington, 2001]. These waves have crests that are oriented perpendicular to the wind direction and propagate in the same direction as the wind, with an additional clockwise offset in the northern hemisphere of about 18° , a slightly larger bias than for roll vortices [Worthington, 2001]. Measured wavelengths commonly range between 2 and 10 km and are generally not dispersive. These waves appear on SAR imagery as parallel

SAR Imaging of the Ocean Surface

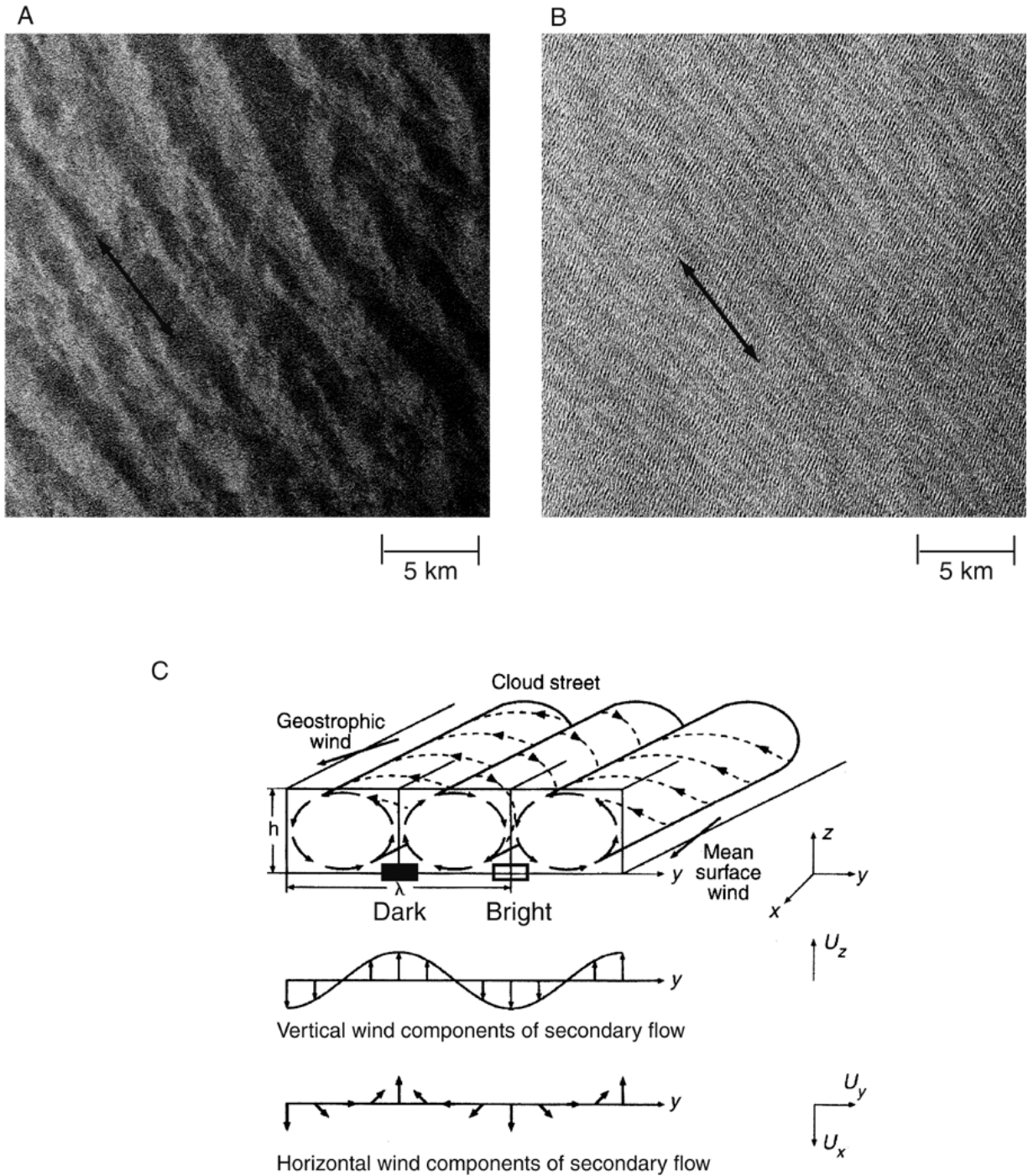


Figure 2.17. Atmospheric roll vortices off Southern California. (a) Large-scale vortices with wavelength spacing on order of 3-5 km (RADARSAT-1, June 12, 1999) and (b) Finer scale vortices with wavelength spacing of 1-2 km (RADARSAT-1, December 2, 1998). The arrows indicate approximate orientation of rolls. (c) Generalized schematic of roll vortices: top, rolls are orientated along the shear vector between the surface and geostrophic wind, and associated radar brightness is associated with downward (bright) and upward (radar) vertical circulation; middle, variation of the vertical component u_z of the wind velocity along the y direction; bottom, variation of the horizontal components u_x and u_y (in the x, y plane). [After *Alpers and Brümmer*, 1994]. New research into rolls has allowed for a more detailed schematic to be produced (See Figure 14.4 in Chapter 14). RADARSAT Images ©CSA 1998, 1999.

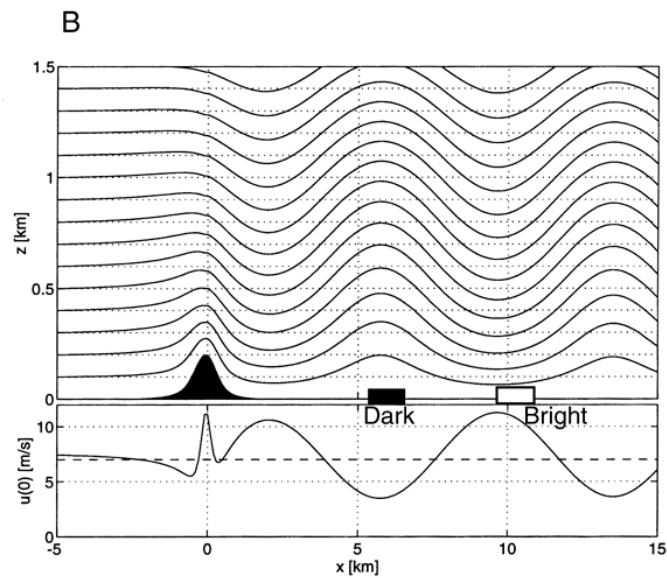
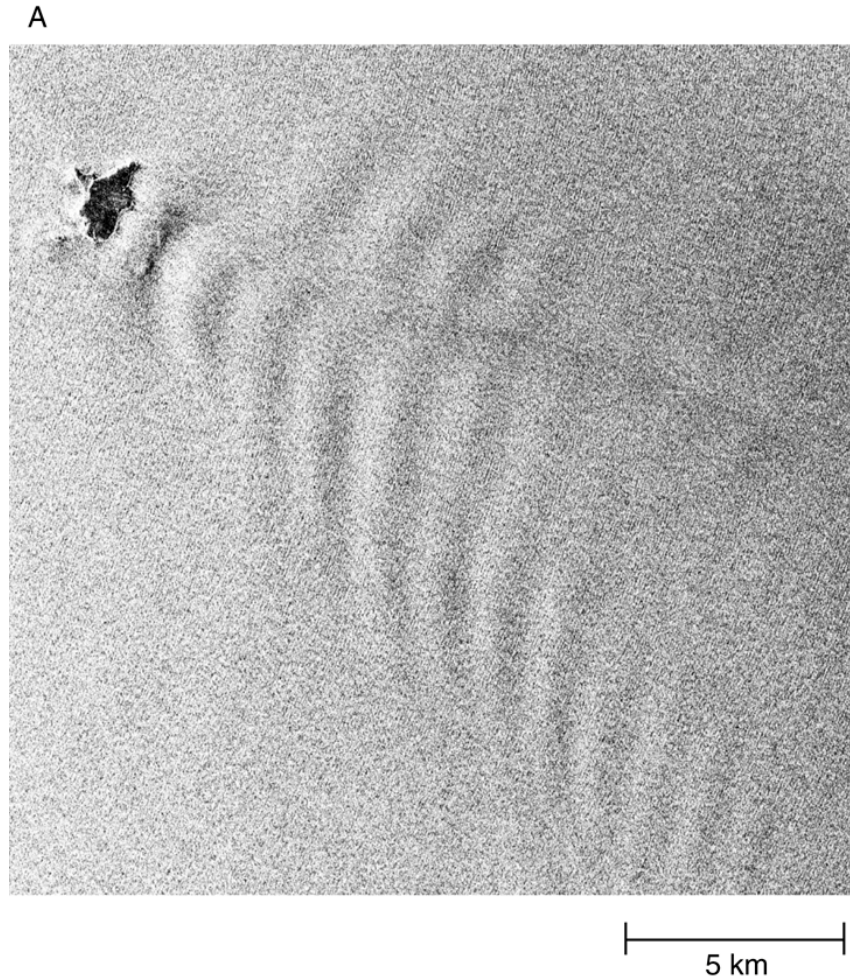


Figure 2.18. (a) Atmospheric lee waves off Santa Barbara Island in Southern California (RADARSAT-1, (C-band, HH) 28 July 1998), (b) Horizontal view of streamlines for one-layer lee waves forming downstream of an island, with the lower scale indicating surface wind speed [After *Vachon et al.*, 1994]. Radar brightness is associated with downward (bright) and upward (radar) vertical circulation. RADARSAT Image ©CSA 1998

SAR Imaging of the Ocean Surface

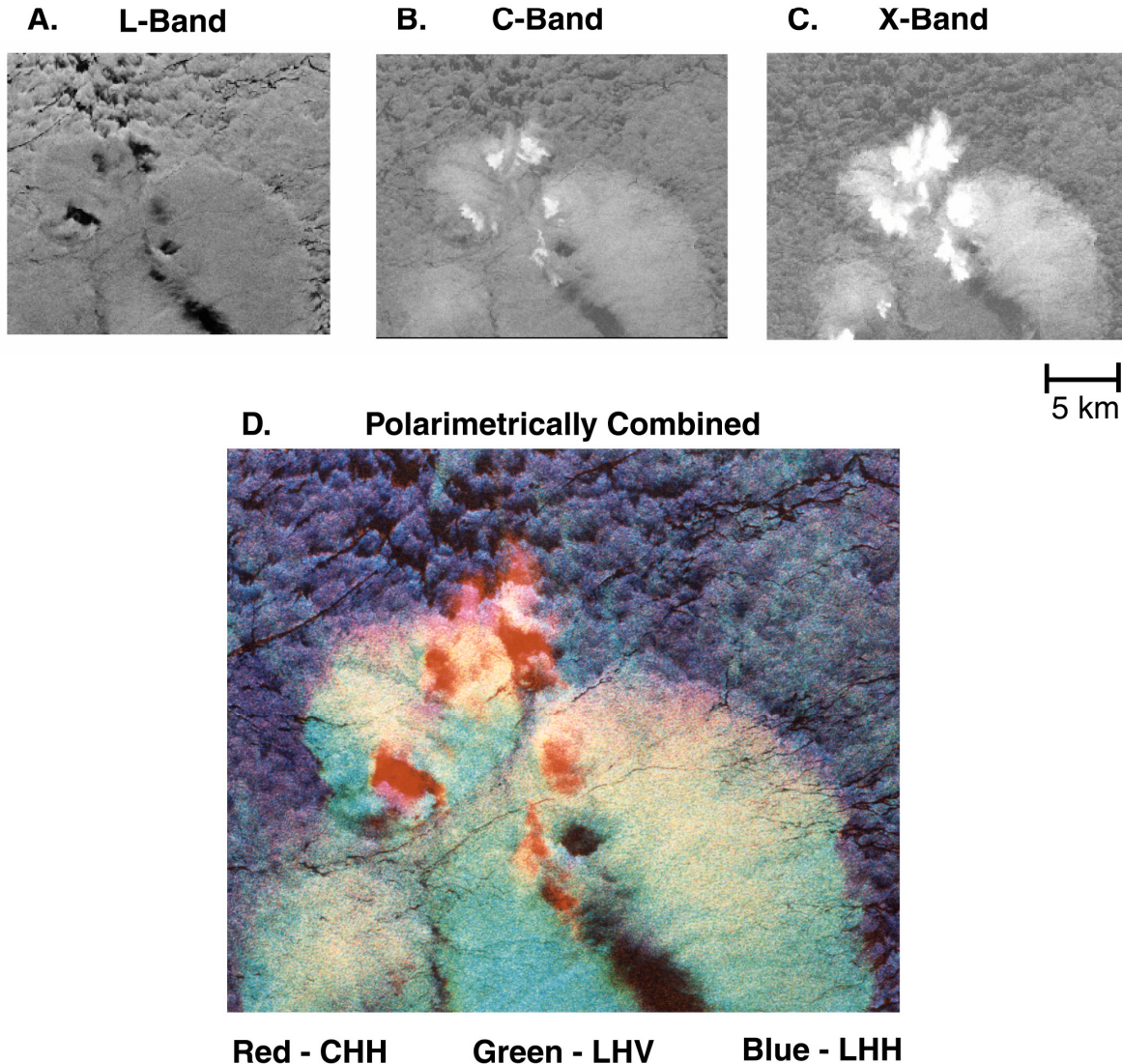


Figure 2.19. SAR images of rain cells obtained by SIR-C/X-SAR on 10 April 1994 near the Ontong Java atoll in the Solomon Islands. The images include (a) L-band, (b) C-band, and (c) X-band, each at VV polarization and incident angles of about 50° . As attenuation and scattering by rain at L-band are small, the variation in surface roughness in (a) is primarily due to wind speed, with the possible additional suppression of backscatter due to wave damping by heavy rain within the dark small cores of each rain cell. The attenuation and scattering from rain increases as the radar frequency increases (a) to (c), particularly over the small dark areas seen on L-band where rainfall may be heaviest. (d) Selected polarization combinations from L-band and C-band data are combined to highlight different scattering components within the above rain cell. LHH highlights the low-wind ocean returns, LHV isolates the high winds within the rain cell, while CHH selectively isolates ice particles within the rain cell. Images (a) to (c) [After Jameson *et al.*, 1997].

wide bands with alternating bright and dark returns, reflective of fluctuating surface wind speeds between the downdraft and updraft portions of the oscillating waves (Figure 2.18). In fact, the SAR signatures and feature scales are similar to roll vortices. Without knowledge of the local wind direction, it may be difficult to distinguish the two features. Recent observations are being examined where both roll vortices and gravity waves occur simultaneously within the same image, providing a unique opportunity to compare the signatures, conditions for formation, and inferred measurements of the boundary layer [Winstead *et al.*, 2002].

2.3.2.4 Rain cells. Rain cells were first identified on SEASAT SAR as bright circular features with a dark center ranging from 2 to 40 km in diameter, with the outer edge being the squall line [Ross, 1981; Fu and Holt, 1982]. More detailed studies attributed the dark core to be associated with heavy rainfall, which damped out short ocean waves, and the bright areas as high-speed radially spreading downdrafts or microbursts [Atlas, 1994]. In later results with C- and X-band imagery (Figure 2.19), the downdraft portion of the rain cells appeared similar, however the dark core was replaced by an inner core that was even brighter than the downdraft portion [Jameson et al., 1997; Moore et al., 1997; Melsheimer et al., 1998, 2001]. At the higher frequencies, the intense rain in the core was found to increase surface roughness rather than dampen surface roughness with an additional scattering contribution from raindrops. Estimates of rain rates have been made based on the SAR signatures [Jameson et al., 1997; Moore et al., 1997; Melsheimer et al., 1998], including within a tropical squall line [Lin et al., 2001]. A recent study with ERS SAR has shown that the inner core can be either bright or dark depending on whether the rain rate is below or above 50 mm h^{-1} , where the higher rain rate reduces the surface roughness in C-band in a similar way as with L-band [Melsheimer et al., 2001].

2.3.2.5 Additional air-sea interactions. The detailed structure of polar lows, which are intense mesoscale cyclonic vortices formed when cold air crosses from sea ice or cold land to the relatively warmer ocean, and hurricanes, including regions of cellular convection and rain bands, have been examined [e.g., Katsaros et al., 2002; Sikora et al., 2000]. The appearance of cellular convection varies on SAR imagery depending on whether the boundary layer is stable or unstable, including differences in air and sea temperatures [Sikora et al., 1995, 1997; Sikora and Thompson, 2002]. Fronts have also been examined [Johannessen et al., 1991; Winstead and Mourad, 2000; Winstead et al., 2002]. Various terrain-related effects on winds have been examined, including gap winds and wakes [Pan and Smith, 1999], katabatic winds [Alpers et al., 1998; Winstead and Young, 2000], and atmospheric vortex streets [Li et al., 2000].

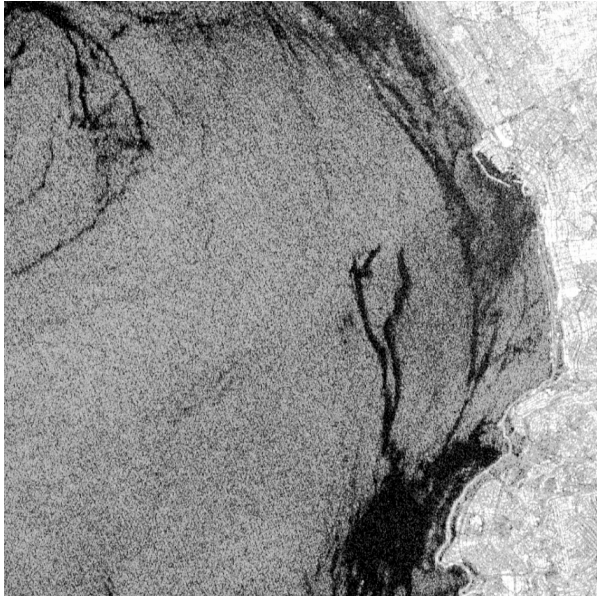
2.3.3 Surface slicks from biogenic and mineral oils

Through convergence, biogenic films are thought to be the primary means by which small eddies and internal waves are imaged on SAR (as well as in sun glint photography) [e.g., Johannessen et al., 1996; Nilsson and Tildesley, 1995; Espedal et al., 1998; Munk et al., 2000; DiGiacomo and Holt, 2001]. The eddy motions align the films into curving parallel bands that trace the underlying current fields. Small or spiral eddies, with scales of 1 to 40 km, appear to aggregate organisms and likely nutrients as well through vertical pumping of nutrient-rich colder water to the photic zone (isopycnal doming in cyclones) (Figure 2.15). Internal waves likewise sweep biogenic films into bands which appear dark and often together with bright bands (Figure 2.13). Only limited in-situ verification of the biogenic films coincident with SAR imagery have been made [e.g., Espedal et al., 1996, 1998].

For mineral oils, SAR time series studies have been used to identify the significant and largely illegal discharge from ships [Gade and Alpers, 1999; Lu et al., 2000; Pavlakis et al., 2001], to develop an inventory of natural seeps in the Gulf of Mexico [MacDonald et al., 1993], and to examine the extent of stormwater and sewage runoff in Southern California [Svejkovsky and Jones, 2001]. A continuing study of Southern California stormwater discharge, that also includes detection of a surfacing sewage plume and entrainment of natural seeps by coastal currents along with comparisons with shore-based high frequency radar and other in-situ measurements, has recently been done [DiGiacomo, et al., 2004]. The use of SAR for

SAR Imaging of the Ocean Surface

A. December 26, 1998 (R1)



B. August 02, 2001(ERS2)



C. January 27, 2002, 0141GMT (R1)



D. January 27, 2002, 1400 GMT (R1)



5 km

Figure 2.20. A series of RADARSAT-1 (R1) (C-band, HH) and ERS-2 (C-band, VV) SAR images of a small natural mineral oil seep off Redondo Beach, Los Angeles County. The seep has two adjacent release points, most clearly seen in (c) and (d). It is not possible to discriminate by backscatter the seep from other nearby dark slicks, which are likely biogenic in origin, in any individual image. However, a time series provides clear indication of the two release points and general extent even when the seep orientation changes in relation to local winds and currents. RADARSAT Images ©CSA 1998, 2002. ERS-2 Image ©ESA 2001

monitoring oil spills has also been examined [e.g., *Fingas and Brown, 1997; Jones, 2001*]. Despite its all-weather, high resolution capability, SAR has limitations for detecting and tracking oil spills which include a non-unique signature (similar to low wind returns), episodic sampling, no estimate of thickness, and difficulty discriminating oil type such as distinguishing biogenic oils from oil spills. Detection algorithms have been developed to improve the separation of oil spills from similarly appearing features that make use of environmental information in interpreting the evolving shape and characteristics of slicks [*Solberg et al., 1999; Espedal and Wahl, 1999*]. Figure 2.20 illustrates how a time series of a small natural seep provides clarification of the seep location, varying extent, and discrimination from surrounding dark regions.

Controlled spills of mineral and artificial biogenic oils have been done to determine radar detection characteristics and imaging mechanisms [e.g., *Wismann et al., 1998; Gade et al., 1998a, 1998b*]. The term ‘damping ratio’ is used to specify the reduction in radar return from the oil-covered surface as compared to the background ocean-only return. In general the damping ratio for both oil types increases from L- to Ku-band, is not sensitive to polarization, decreases with increasing incident angle, and decreases with increasing wind speed. The damping ratio increases with viscosity and thickness of mineral oils, and heavy oils are detectable under higher winds than lighter oils [*Wismann et al., 1998*]. At C- and X-bands the damping ratios are quite similar for both forms of oil [*Gade et al., 1998a*]. The only exception to these trends is that at L-band, natural biogenic (but not artificial) films over relatively large areas appear to have higher damping ratios than mineral oils, thus suggesting that multiple frequencies may be able to discriminate both oil types [*Gade et al., 1998a; Trivero et al., 1998*].

A summary of the imaging mechanisms [*Gade et al., 1998b*] indicates that for biogenic oils, the Maragone resonance effect accounts for damping ratios at low Bragg wave numbers and moderate wind speeds. The Maragone effect takes place when energy from capillary-gravity waves goes into compressing and elastic stretching of the film, forming surface tension gradients (Maragone waves) which further attenuate the short waves. However, at intermediate to higher Bragg wave numbers and increasing wind speeds, additional energy from wind effects to the wave spectrum are needed to account for the increase (rather than expected Maragone decrease) in damping ratios. Damping in mineral oils is accounted for by viscosity, except at high winds and Bragg wavenumbers, where the additional wind-wave terms likewise provide better fits to measurements. The appearance of oil slicks on SAR imagery depends on environmental conditions (wind, waves, currents, tides) as well as radar system parameters (frequency, polarization, incident angles etc.) [*Gade et al., 1998a; Trivero et al., 1998*]. Under higher winds, the appearance of biogenic oil on SAR images including that contained within convergent zones of small eddies appears to disperse when wind speeds exceed 7 to 8 m s⁻¹ [e.g., *DiGiacomo and Holt, 2001*]. Mineral oils may be detectable on SAR imagery until winds exceed 10 to 14 m s⁻¹, depending on sea state and heaviness of oil [e.g., *Espedal et al., 1996, 1998; Wismann et al., 1998*].

2.4 Special Topics

2.4.1 The Use of Multiple Radar Frequencies and Polarizations

As with all remote sensing, the use of multiple channels of information enables optimization for differentiation and/or highlighting of specific features of interest. For SAR, combining multiple frequencies and polarizations effectively isolates different scattering

characteristics, which improves the interpretation of the SAR ocean signatures and hence understanding of the underlying ocean physics. To date, only the SIR-C/XSAR missions, SRTM, and certain aircraft systems have provided integrated multi-frequency/multi-polarization SAR systems and data. ENVISAT is the first free-flyer orbiting SAR to include dual polarization capability. Multiple SAR channels add considerable power and mass (i.e., cost) to a system, which to date have both been more readily accommodated on the shuttle platform than satellite platforms. We will first discuss frequency followed by polarization, including the more specific implementation of polarimetry. Some aspects of these topics have been discussed earlier in the chapter.

Across the range of common SAR frequencies (P-band to Ku- band, 0.5 to 13 GHz), in general it can be said that lower frequencies (P- and L-bands) are more suited for detecting wave-current interactions (the ‘ocean channels’) while the higher frequencies (X- and Ku- bands) are more responsive to wind variations (the ‘weather channels’) [e.g., *Ufermann and Romeiser, 1999; Lyzenga, 1998*]. This is based on the general notion that wind field variations over short time and space scales primarily modulate short surface waves (Bragg scatterers) and wave-current interactions primarily modulate longer waves. Imagery from C-band provides satisfactory detection of the broadest range of ocean applications, as it is responsive to both current and wind variations. However, C-band imagery by itself, being useful for both ocean and air-sea features, also has some inherent confusion in the clear differentiation of signatures because of contributions from multiple scattering components often simultaneously present on the ocean surface. The differences between frequencies for current- and wind-related features were alluded to in the discussion on short wave interactions with currents (Section 2.2.4). Wave-current interaction models for L-band models generally are satisfactory but models for higher frequencies call for the incorporation of intermediate-scale waves [*Thompson, 1988; Lyzenga, 1998; Romeiser and Alpers, 1997*]. The use of multiple frequencies by themselves has been shown to significantly improve the interpretation of SAR ocean imagery as compared to a single frequency [e.g., *Jameson et al., 1997; Melsheimer et al., 1998; Chubb et al., 1999; Ufermann and Romeiser, 1999*] by isolating atmospheric and oceanic responses (Figure 2.19). The ability to isolate signatures and contributions becomes even more powerful with the use of multiple polarizations.

Polarization differences in radar ocean backscatter were noted in section 2.2.2 and Figures 2.5 and 2.6, where horizontal and vertical polarization combinations of transmit and receive were shown to vary with frequency, incident angle, and wind speed as well as in relation to radar imaging geometry and wind direction [*Ulaby et al., 1982, 1986; Unal et al., 1991*]. Two-scale or composite scattering models, which account for Bragg scatter of short waves present on longer waves under a fully developed sea, generally account for these differences [e.g., *Valenzuela, 1978; Donelan and Pierson, 1987; Romeiser et al., 1997*]. The fact that VV ocean backscatter returns are nearly always larger than HH returns provides a fundamental relationship that has been significantly exploited particularly for measuring ocean wind speeds. The differences between VV and HH increase with increasing incident angle, peaking at C-band, which is attributed to VV being less sensitive than HH to the local tilt of scattering facets riding on the longer gravity waves. The difference between VV and HH is largest at low winds and decreases steadily with increasing wind speed, indicating that HH is more sensitive to wind speed than VV. It has been identified that HH is more sensitive to whitecaps and wave steepness than VV. Differences between measurements and the two-scale models have been attributed to contributions from wedge scattering and wave breaking at high incident angles and specular

scattering at near-nadir angles [e.g., *Valenzuela*, 1978; *Donelan and Pierson*, 1987]. We also note the more recent work on bound waves which provide additional improvement for knowledge of sea surface scattering at varying imaging geometries [*Plant*, 1997, 2002].

Much less is known about the polarization signatures of wave-current interactions, since there is a general lack of suitable SAR data for such studies, as compared to the more extensive scatterometer/SAR data that is available for examining surface roughness primarily related to air-sea interactions. However, studies that use valuable but limited multiple frequency/polarization data, including from SIR-C/XSAR and the NASA/JPL AIRSAR instrument, have provided critical insight on polarization signatures of the ocean surface and current feature detection.

Most of these studies make use of a technique called radar polarimetry, whereby multiple polarizations are simultaneously obtained, providing coherent observations of surface reflectivity from separate polarizations. The polarizations are combinations of horizontal or vertical polarizations in transmit or receive modes (HH, VV, VH, HV). With a coherent polarimetric radar, both phase and amplitude information are available for each pixel as a scattering matrix [*van Zyl et al.*, 1987; *Zebker et al.*, 1991; for a succinct summary, see *Raney*, 1998]. From the scattering matrix, full transformation of the polarization state can be used to seek unique polarization signature(s) of a particular type of surface feature. These signatures can then be used to compare with and improve scattering models, including Bragg and hydrodynamic components, to improve the understanding of the ocean physics and what the radar is actually detecting. This technique helps unravel whether a signature is arising primarily from air-sea interactions and/or wave-current interactions and at what polarization-frequency combination these signatures are enhanced or most clearly isolated from one another.

Using both AIRSAR and SIR-C data, a series of studies over the Gulf Stream [*Shuler et al.*, 1993; *Lee et al.*, 1998; *Chubb et al.*, 1999; and *Ufermann and Romeiser*, 1999] has investigated the widely varying signatures across the current. Of particular note is that despite the lower radar returns, HV/VH polarimetric signatures at the Gulf Stream temperature front are enhanced compared to those of VV and HH, particularly at L-band. This enhancement is due to the impact of mean square surface slope of waves longer than Bragg being strongest at HV/VH, where the radar cross section is lowest, in contrast with HH and VV being impacted primarily by radar cross section. Better match-ups with theory and signatures were realized by accounting for the varying wave spectra evolution (wave action) [*Chubb et al.*, 1999] and most completely with varying currents, wind field, and boundary layer stability [*Ufermann and Romeiser*, 1999]. In other studies using multi-parameter SAR data, *Gade et al.*, [1998a] found that it may be possible to separate mineral and biogenic oils using multiple frequencies at low to moderate wind speeds while *Jameson et al.*, [1997] and *Melsheimer et al.*, [1998] found that phase differences between HH and VV copolarization signals indicate the possibility of measuring rain rate.

2.4.2 Currents and Wave Spectra from Along-Track Interferometry

Along-track interferometry (ATI) is a unique SAR configuration which enables the velocity of the moving ocean surface to be measured over a very short time interval. Such data have been examined for deriving wave spectra and current velocity, to date primarily from aircraft platforms. By careful tracking of multiple SAR observations of a single target on the ocean surface, the displacement or motion of the target can be determined by measuring the phase difference between the observations and after removal of other systematic motions. Nominally, the platform is configured with a fore and aft radar antenna along the fuselage or platform velocity direction, where either one or both antennas transmit and both antennas receive

SAR Imaging of the Ocean Surface

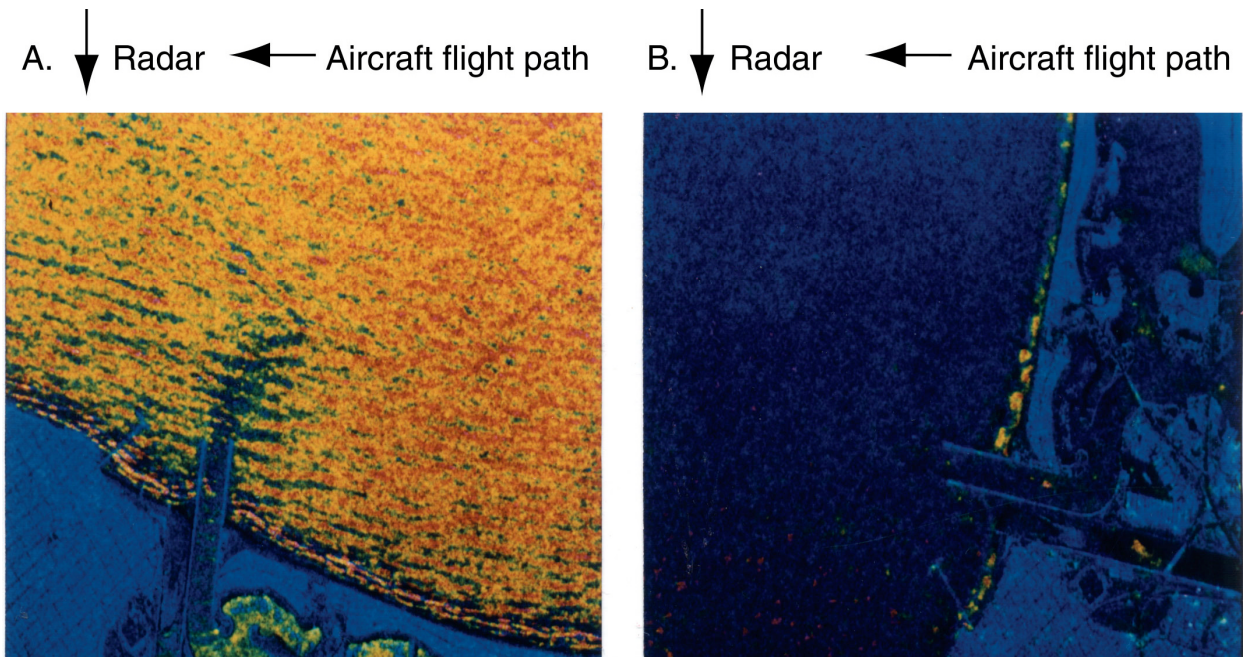


Figure 2.21. Aircraft SAR interferogram pair of Mission Bay near San Diego with 90° difference in imaging aspect angle, illustrating along-track interferometry and detection of surface currents. The color code is as follows: light blue on land represents no motion, yellow is for motion away from the radar, and deep blue/magenta for motion towards the radar. In (a) the outgoing tidal flow is deep blue/magenta and shoreward-traveling wind-driven Bragg waves are yellow. When the flight path is rotated 90° (b), the tidal flow is now along-track and does not appear, while the Bragg wind wave field has a noticeable component toward the radar (dark blue). [After *Goldstein et al.*, 1989].

the returns with a conventional side-looking radar beam. In this case, the radial (or line-of-sight) velocity, v , of a target is based on the following relation,

$$v = \Delta\phi \lambda_r V / 2\pi d \quad (7)?$$

where $\Delta\phi$ is the observed phase change of the surface scatterer, λ_r is the radar wavelength, V is the platform velocity, and d is the distance (or baseline) between the two antennas. The time lag, τ , between forward and aft imaging is d/V . The time lag must be smaller than the ocean decorrelation time or the targets will lose phase coherency and smear. The incident angle on the ground is accounted for by dividing by $\sin(\theta)$. Recalling that the Bragg number, λ_B , is given by $\lambda_r/2 \sin \theta$, it follows that

$$v = \Delta\phi \lambda_B / \tau\pi. \quad (8)?$$

The phase change arises from contributions from the wave orbital velocity, the surface current, and wind.

Aircraft ATI measurements have been used to derive surface currents (Figure 2.21) [Goldstein and Zebker, 1987; Goldstein et al., 1989; Ainsworth et al., 1995; Marmorino et al., 1997] including comparisons with high frequency coastal radar [Graber et al., 1996], to examine ocean waves [Marom et al., 1991; Vachon et al., 1999], and internal wave currents [Thompson and Jensen, 1993]. A numerical study examined several radar configurations and varying current and wind fields and determined that the best results would be obtained at high

frequencies (X-band better than L-band), high viewing angles, vertical polarization and low platform altitude/speed ratios [Romeiser and Thompson, 2000]. Coherence time, which varies by frequency, incident angle and polarization, ranges from roughly 0.1 to 0.3 seconds for L-band [Carande, 1994; Shemer and Marom, 1993] to 0.001 to 0.002 for X-band [Plant et al., 1994]. Increasing wind speed tends to reduce the coherence time [Frasier and Camps, 2001].

Aside from the general difficulty of sorting out the various contributions to the target motion as well as the systematic contributions from the platform and processing, one of the drawbacks of the nominal, side-looking two-antenna system is that only the line-of-sight radial component of the motion field is derived during a single imaging event. The full surface motion vector would thus require at minimum two perpendicular crossing acquisitions with minimal separation in time to avoid further ocean decorrelation. Recent studies have examined the concept of a pair of beams using dual antennas to squint forward and squint aft (dual aspect) of the nominal side-looking antenna beam [Moller et al., 1998; Frasier and Camps, 2001]. By aligning these measurements, the full surface velocity vector may be obtained within a single acquisition. Such a concept might be particularly adaptable to a spaceborne system, perhaps by using a split-beam single antenna, thus enabling current/motion measurements from a single spacecraft rather than a tethered-dual spacecraft concept [Moccia and Ruffino, 2001]. In an alternate concept, across-track interferometry has been demonstrated that can produce a digital elevation map of the ocean surface height, useful for measuring waves [Schulz-Stellenfleth et al., 2001] and mesoscale eddies [Rodriguez et al., 2003].

2.4.3 SAR Spatial and Temporal Sampling

The fine resolution, detailed views of the ocean surface obtained by SAR are tempered by the fact that spaceborne SAR sensors have limited duty cycles, which results in periodic imaging usually separated by a few days over a given location. The duty cycle, or time that a SAR can operate per orbit, is limited by instrument power requirements, data rates, and, until recently, data storage. There is always a trade-off between swath width and resolution in SAR systems as well. Most of the ocean features best detected by SAR have shorter temporal scales than the SAR revisit intervals which generally range from 3 to 5 days or longer depending on latitude (see Chapter 1 and Appendix A). Over specific sites, it is possible to get 12-hr repeat sampling provided the SAR is able to operate both during descending and ascending portions of an orbit (such as RADARSAT-1 which is in a dawn-dusk sun-synchronous orbit). Even 12-hour repeat imaging may be subject to local diurnally-varying winds, which may prove less effective than repeat sampling at the same time of day. The comparatively narrow swath widths (100 to 500 km) of SAR provides further complications as compared with other standard ocean sensors (except radar altimeters), which have swath widths between 500 and 3000 km and thus provide 12-hr to 2-day revisit intervals of the entire globe, albeit at coarser resolutions than SAR. The best case scenario for obtaining large regional mosaics over short time scales is in the polar regions. For example, the mapping of the entire Arctic ocean every three days is routinely accomplished using RADARSAT-1's wide swath mode, making use of the converging orbits in the polar regions. Equivalent mapping at lower latitudes takes longer. Another key constraint on sampling is that spaceborne SARs point to one side of the spacecraft (not a limitation in previous shuttle missions), which limits the accessible field of view. One clear consequence of this limited view is in the polar regions, where the nominal right-hand side view of all spaceborne SARs flown to date enables nearly complete viewing of the Arctic while precluding imaging of the Antarctic continent except along the continental margins, depending upon orbit inclination.

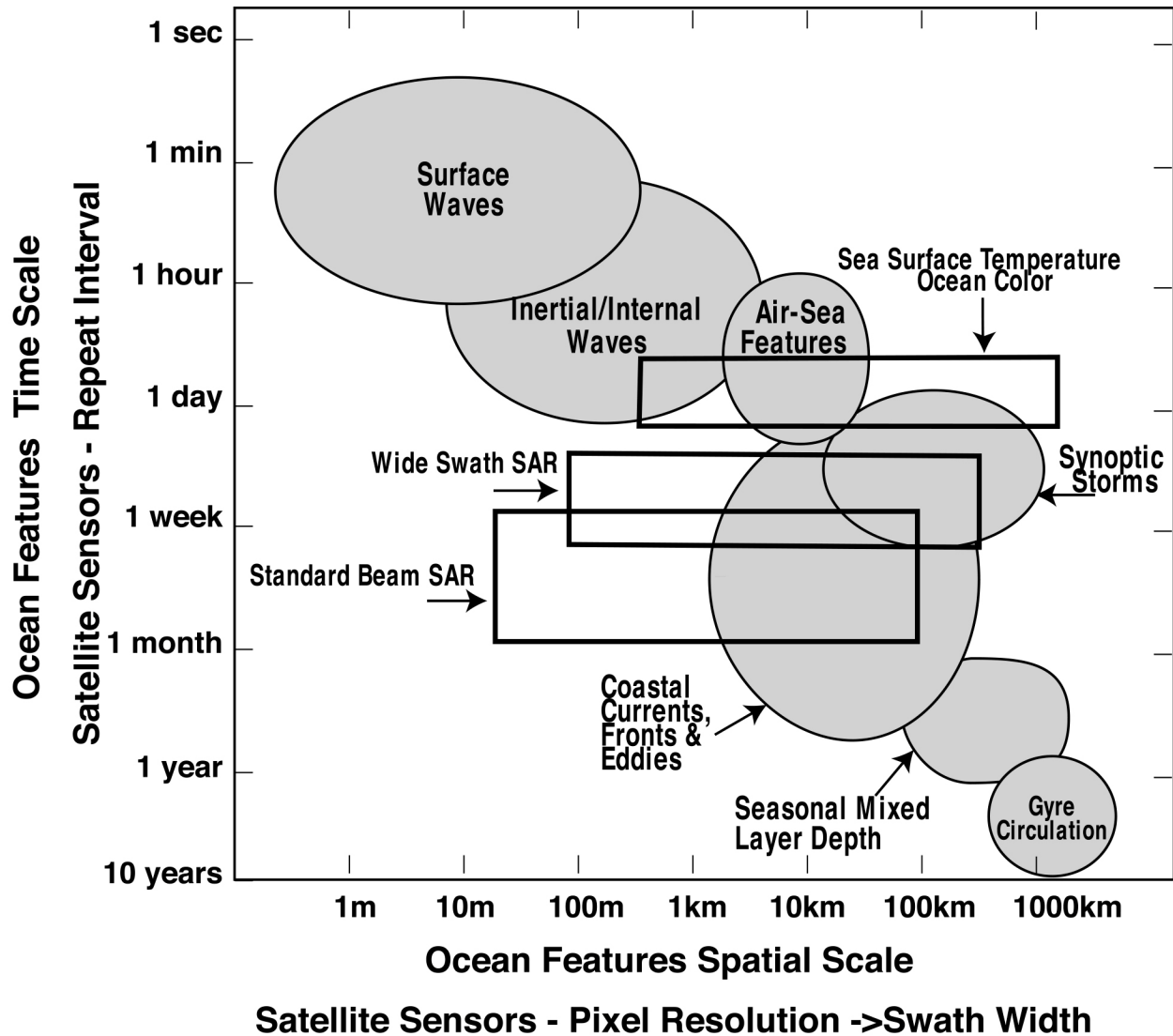


Figure 2.22. Satellite spatial and temporal sampling of ocean features. The bubbles indicate both the spatial and temporal scales of variability of a range of ocean features [adapted from *Dickey*, 1991], with particular focus on those commonly imaged by SAR. The boxes indicate length and time scales for standard sensors for sea surface temperature and ocean color (e.g. AVHRR, SeaWiFS, MODIS, ENVISAT AATSR and MERIS), and both nominal standard beam and wide swath SAR modes (e.g. SEASAT, ERS-1/2, JERS-1, RADARSAT-1, ENVISAT ASAR). The satellite length scale axis extends from the pixel resolution up to swath width, while the time scale axis includes approximate repeat intervals which varies by latitude and orbit [adapted from *Robinson*, 1997]. Note that to improve the general undersampling by SAR of the types of ocean features that it best measures requires either multiple satellites and/or improved swath coverage (see text for further description).

In Figure 2.22, we attempt to synthesize these sampling issues. Regarding ocean features first, we have condensed a more extensive illustration of timescales of ocean physical processes from *Dickey* [1991] to highlight primarily those features detected by SAR that we have discussed (listed in Table 2.1). The satellite coverage for both generic standard beam and wide swath spaceborne SAR modes and sea surface temperature/ocean color sensors are overlaid, with the primary purpose of illustrating the temporal repeat interval of each sensor type. The comparatively limited sampling of a SAR will make it difficult to perform some studies, such as

the evolution of surface waves within a storm or the life cycle of smaller eddies, for example. When the vagaries of detectable range of favorable wind speeds are factored in, it makes the case of developing satisfactory time series with a SAR difficult.

How can improved sampling of the ocean surface with SAR be achieved? The first obvious answer is the use of multiple SAR spacecraft, such as exists at the time of this writing with RADARSAT-1, ENVISAT ASAR, and ERS-2 SAR. In the near future, the launch of ALOS PALSAR and RADARSAT-2 will further augment the imaging opportunities. Referring back to Figure 2.22, two wide swath SAR spacecraft would move the repeat interval upward on the graph by 1 to 2 days. The RADARSAT-2 antenna will be configurable to image either side of the satellite track, which greatly improves the accessible field of view for imaging targets of opportunity and both polar regions. In the above situations, each SAR satellite has different frequency and polarizations, optional modes and viewing angles. In addition, coordination with multiple flight agencies is required and the repeat sequences will be highly variable with the different orbital repeat cycles, optional modes and viewing angles.

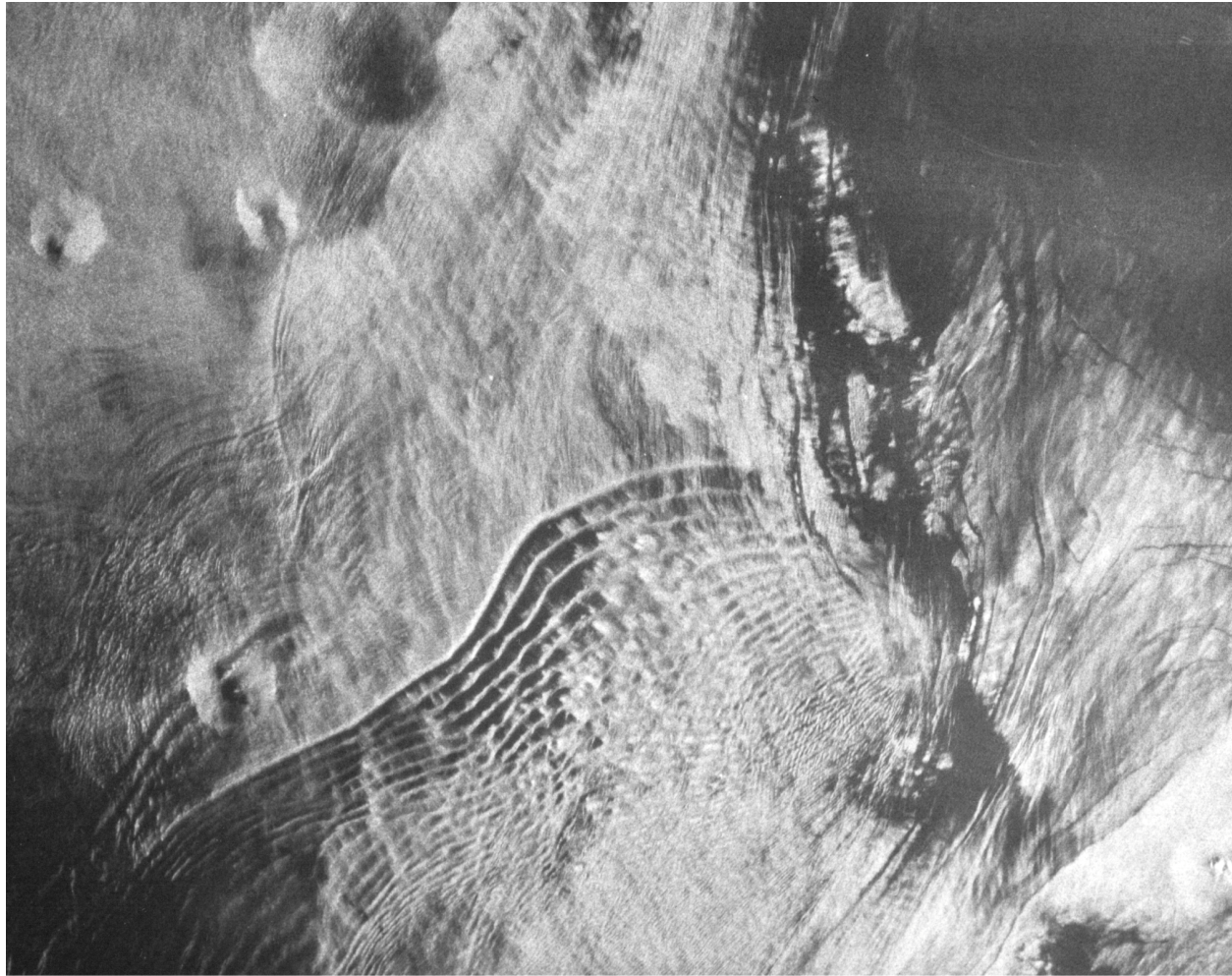
In a recent study, *Holt and Hilland* [2000] examined several additional satellite options: 1) to extend the swath width up to 800 km with a single antenna, while maintaining an acceptable range of incident angles, by placing the satellite in a higher than normal sun-synchronous orbit (about 1350 km as compared to about 800 km); 2) a single spacecraft carrying two antennas in a conventional sun-synchronous orbit (about 800 km); and 3) a geosynchronous satellite which could provide daily coverage of limited regions. In option 1, a three-day repeat orbit provides nearly complete coverage at the equator while a second satellite in a duplicate orbit offset by one day would further reduce the repeat interval to 1-2 days. In option 2, a five-day exact repeat orbit cycle provides nearly global coverage using two- and three-day subcycles within the five-day repeat. A second satellite offset by one orbit would reduce the repeat interval to 12 to 24 hr. Each option, however, would require a costly technological advancement compared to current conventional SAR systems.

In summary, at least two SAR spacecraft with wide swath imaging capabilities are needed to improve the sampling of the spatial and temporal variability of the key ocean features imaged by a SAR. In the best of all possible worlds, these multiple spacecraft would have identical instrument configurations, be placed in similar orbital sequences to maximize coverage and minimize repeat intervals, and operate under a unified set of imaging requirements over a specific region.

2.4.4 Summary with Case Studies

As a means of summarizing what has been presented, we show three final but complicated SAR images, to illustrate the comparative scales of the various detected surface features, how the features may appear simultaneously and overlapping with each other, and to provide an example of what remains to be learned oceanographically that can likely only be detected with SAR imagery.

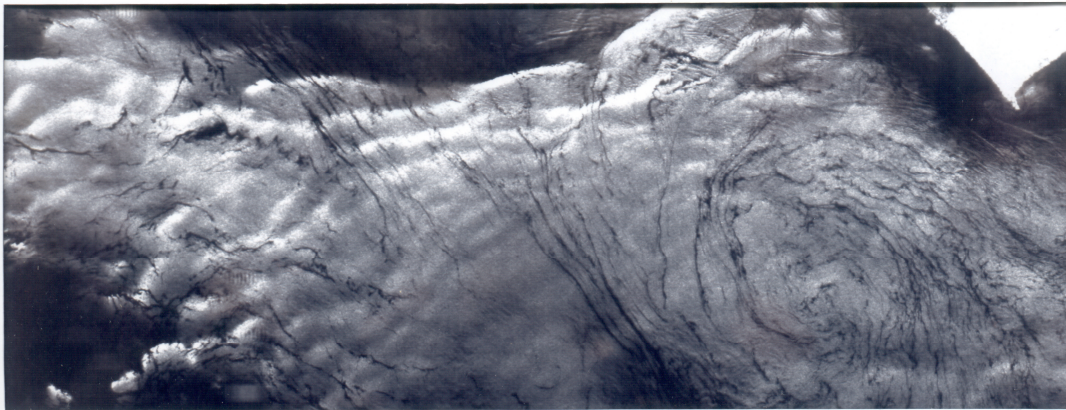
Numerous ocean and atmospheric features present in the Gulf of Mexico are seen in Figure 2.23. This image is located northeast of the Yucatan Peninsula, where the Loop Current enters the Gulf through the deeper Yucatan Channel, hugging the continental shelf which extends north of the peninsula. The image is dominated by an extensive internal wave packet in the lower center. The leading wave crest is over 50 km long and has over 10 successive wave crests with decreasing wavelengths which are indicative of wave dispersion. Note the strong contrast in radar signatures in the internal waves, with most waves composed of an enhanced bright band



10 km

Figure 2.23. SEASAT (L-band, HH) SAR image of the Gulf of Mexico showing internal waves, rain cells, current patterns, and cellular convection (24 August 1978).

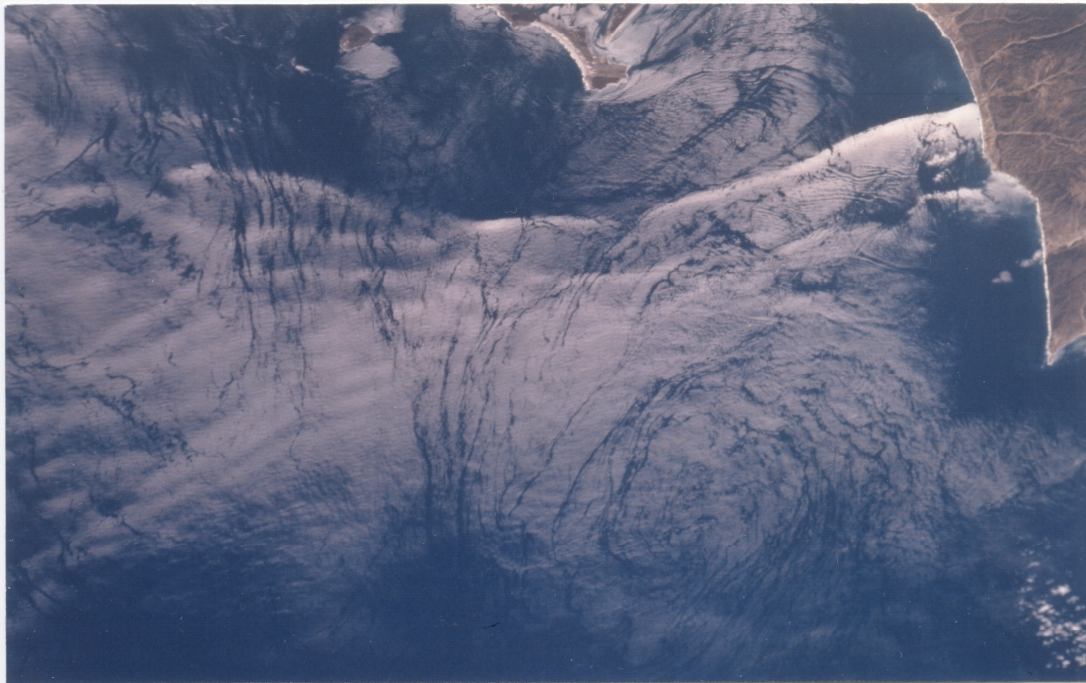
in front adjacent to a suppressed dark band. To the upper left of the large packet are additional packets composed of finer-scale internal waves. The packets are propagating across the shelf from the deep water channel. Also apparent on the left side are at least three circular rain cells between 5 and 7 km in diameter, with each main cell being brighter and enclosing a smaller central core that is darker than the surrounding ocean. In the lower right quadrant, the linear dark striations are indicative of the presence of a surface current field, likely the Loop Current, as well as a small spiral eddy adjacent to more linear striations (right center). The dark striations are most likely biogenic surfactants aligned by the current. Note the highly varying wind-induced roughness patterns throughout, including the large dark region in the upper right and the patches of bright and dark also seen within the large internal wave packet. Interesting questions one might ask are why the scale of internal water packets are so variable and whether the dark region is indicative of a sharp temperature change that may have increased the boundary layer stability and thus enhanced roughness.

L-BAND TOTAL POWER IMAGE

SRL-2 DT 168.6

LAT 30.1°N LON 116.1°W OCT 10, 1994

10 km

HASSELBLAD HAND-HELD SUN GLINT IMAGE

ROLL 260 – FRAME 30

Figure 2.24. Comparison of SIR-C (STS-068) L-band total power SAR image and coincident shuttle sun glint photograph of a small-scale eddy and atmospheric gravity waves off the west coast of Baja California (October 10, 1994). The images are not co-registered (see land in upper right corner) and thus not aligned.

sun glint spot, a spot detectable from an airplane or space shuttle where the sun is reflected off the surface to a human eye (i.e., the angle of the sun and the eye to the feature are equal but opposite). This is illustrated beautifully in Figure 2.24 off the western coast of Baja California, showing a comparison of a coastal spiral eddy (dark curvilinear striations) and atmospheric gravity waves (bright broad waves extending lengthwise across image) as seen with a SIR-C L-band total power image and a coincident hand-held sun glint photograph taken from the space

SAR Imaging of the Ocean Surface

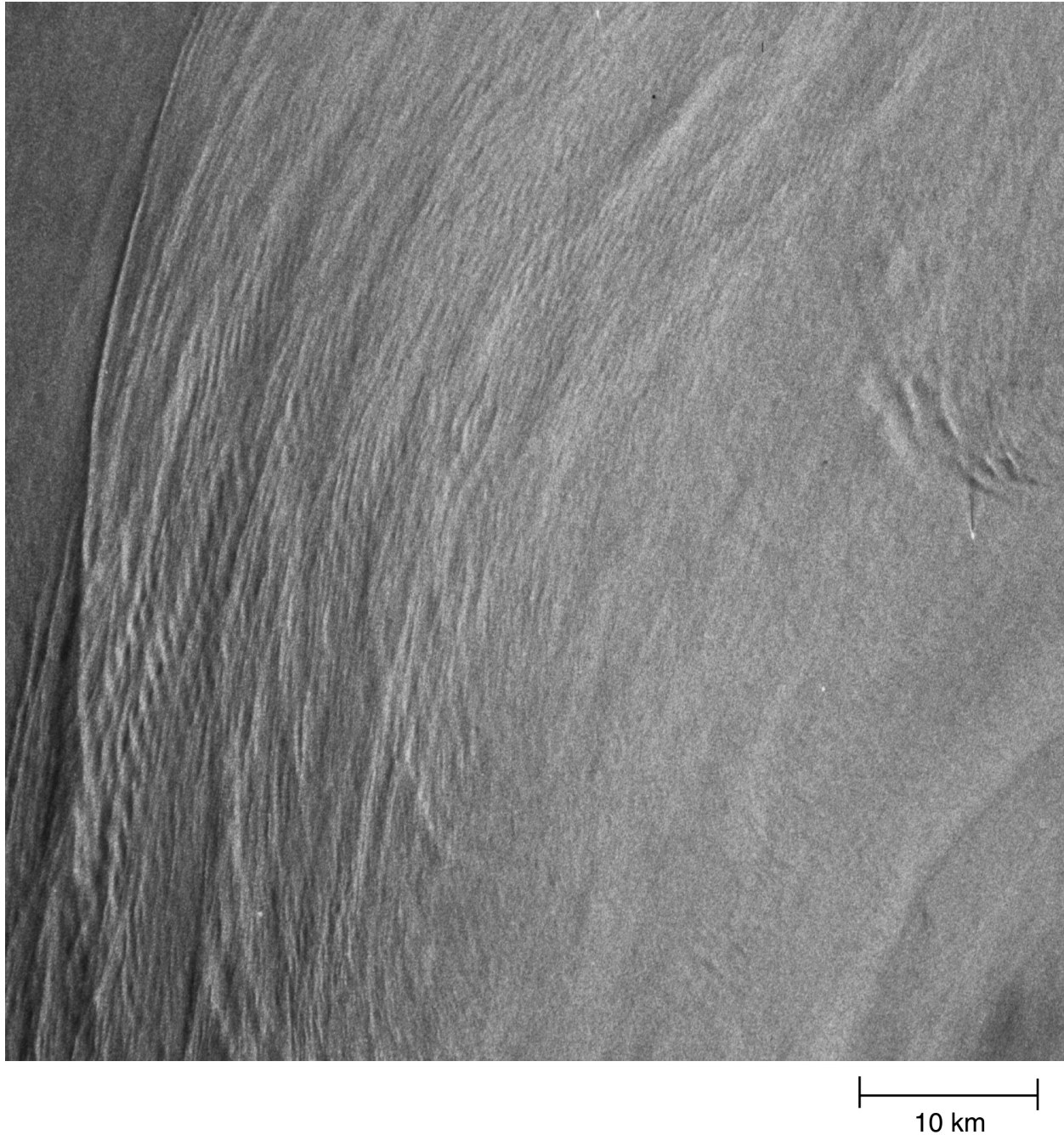


Figure 2.25 SEASAT (L-band, HH) SAR image of the Gulf Stream, with unusual wave patterns contained within the confines of the main current (25 July 1978).

shuttle. In this case, the bright regions and dark regions largely match in both images. In a slightly different sun glint viewing geometry, the bright and dark regions may be opposite to one another, as a smoother surface may appear bright in sun glint imagery (full reflection back to eye) and dark in SAR. While not shown in this image, the unusual atmospheric wave expressions extended a considerable distance off the California coast from Santa Barbara, begging the question as to what meteorological conditions were present that day

The last image (Figure 2.25) appeared in the SEASAT SAR ocean atlas [*Fu and Holt*, 1982, page 47], which shows the breadth of the Gulf Stream off South Carolina. The dark line in the lower right corner delineates the south wall of the Gulf Stream and the north wall is in, or at least adjacent to, the distinct linear feature in the upper left corner. As indicated in the original figure caption, the finer-scale linear striations are trapped along the northern half of the current, have wavelengths between 300 and 1200 meters and crests parallel to the current flow. We believed then, and it is still likely the case now, that these features have not been observed by in-situ measurements and so essentially nothing is known about the physics of the striations. Yet the striations dominate the image and are indicative at minimum of a very complicated, non-uniform current flow field. A plausible explanation may be given in *Mollo-Christensen* [1981], who proposed that such striations were surface effects of the adjustment of the bottom boundary layer to changes in the interior current flow, but to date this has remained unverified with surface measurements, as best as can be ascertained.

The remainder of the book chapters will delve into considerable detail on these primary features that have only been initially described here. There remains much to explore in SAR ocean images, that can produce valuable contributions to the understanding of physical oceanography and the boundary layer, extending into interactions with sea ice, biological processes, and human influences related to pollutants, fishing, and shipping.

2.5 Acknowledgements

This work was supported by the National Aeronautics and Space Administration through a contract with the Jet Propulsion Laboratory, California Institute of Technology. The author would like to thank Bill Pichel for the invitation to write this chapter, Chris Jackson for his considerable patience, Paul DiGiacomo for valuable discussions particularly regarding figure selection, Nettie Labelle-Hamer at the Alaska Satellite Facility (ASF) for additional support, ASF for providing the RADARSAT-1 imagery through a memorandum of understanding between NASA/NOAA and the Canadian Space Agency, and the European Space Agency for the provision of ERS SAR imagery. All the NASA SAR imagery is in the public domain.

2.6 References

- Ainsworth, T. L., S. R. Chubb, R. A. Fusina, R. M. Goldstein, R. W. Jansen, J.-S. Lee, and G. R. Valenzuela, 1995: INSAR imagery of surface currents, wave-fields, and fronts. *IEEE Trans. Geosci. Remote Sens.*, **33**, 1117–1123.
- Alpers, W., 1983a: Imaging ocean surface waves by synthetic aperture radar—A review. *Satellite Microwave Remote Sensing*, T. D. Allan, Ed., Ellis Horwood Ltd., 107-119.
- , 1983b: Monte Carlo simulations for studying the relationship between ocean waves and synthetic aperture radar image spectra. *J. Geophys. Res.*, **88** (C3), 1745–1759.
- , and I. Hennings, 1984: A theory of the imaging mechanism of underwater bottom topography by real and synthetic aperture radar. *J. Geophys. Res.*, **89**, 10 529–10 546.
- , and C. Bruening, 1986: On the relative importance of motion-related contributions to the SAR imaging mechanism of ocean surface waves. *IEEE Trans. Geosci. Remote Sens.*, **24**, 873–885.
- , and B. Brümmer, 1994: Atmospheric boundary layer rolls observed by the synthetic aperture radar aboard the ERS-1 satellite. *J. Geophys. Res.*, **99**, 12 613–12 621.

- , and G. Stilke, 1996: Observation of a nonlinear wave disturbance in the marine atmosphere by the synthetic aperture radar aboard the ERS 1 satellite. *J. Geophys. Res.*, **101** (C3), 6513–6525.
- , D. B. Ross, and C. L. Rufenach, 1981: On the detectability of ocean surface waves by real and synthetic aperture radar. *J. Geophys. Res.*, **86** (C7), 6481–6498.
- , U. Pahl, and G. Gross, 1998: Katabatic wind fields in coastal areas studied by ERS-1 synthetic aperture radar. *J. Geophys. Res.*, **86**, 6481–6498.
- Apel, J. R., 1987: *Principles of Ocean Physics*. Academic Press, 631 pp.
- , and F. I. Gonzalez, 1983: Nonlinear features of internal waves off Baja California as observed from the Seasat imaging radar. *J. Geophys. Res.*, **88**, 4459–4466.
- Atlas, D., 1994: Footprints of storms on the sea: A view from spaceborne synthetic aperture radar. *J. Geophys. Res.*, **99**, 7961–7969.
- Barnett, T., F. Kelly, and B. Holt, 1989: Estimation of the two dimensional ocean current shear field with a synthetic aperture radar. *J. Geophys. Res.*, **94**, 16 087–16 096.
- Beal, R. C., Ed., 1991: *Directional Ocean Wave Spectra*. Johns Hopkins University Press, 218 pp.
- , and W. G. Pichel, Eds., 2000: Coastal and Marine Applications of Wide Swath SAR. *Johns Hopkins APL Tech. Dig.*, **21**, 184 pp.
- , P. S. DeLeonibus, and I. Katz, Eds., 1981: *Spaceborne Synthetic Aperture Radar for Oceanography*. The Johns Hopkins University Press, 215 pp.
- , D. G. Tilley, and F. M. Monaldo, 1983: Large- and small-scale spatial evolution of digitally processed ocean wave spectra from Seasat synthetic aperture radar. *J. Geophys. Res.*, **88** (C3), 1761–1778.
- , T. W. Gerling, D. E. Irvine, F. M. Monaldo, and D. G. Tilley, 1986: Spatial variations of ocean wave directional spectra. *J. Geophys. Res.*, **91** (C2), 2433–2449.
- Bock, E. J., and N. M. Frew, 1993: Static and dynamic response of natural multicomponent oceanic surface films to compression and dilation: Laboratory and field observations. *J. Geophys. Res.*, **98** (C8), 14 599–14 617.
- Brown, R. A., 1980: Longitudinal instabilities and secondary flows in the planetary boundary layer: A review. *Rev. Geophys.*, **183**, 683–697.
- Brown, R. A., 2000: Serendipity in the use of satellite scatterometer, SAR, and other sensor data. *Johns Hopkins APL Tech. Dig.*, **21**, 21–26.
- Carande, R. E., 1994: Estimating ocean coherence time using dual-baseline interferometric synthetic aperture radar. *IEEE Trans. Geosci. Remote Sens.*, **32**, 846–854.
- Chubb, S. R., and Coauthors, 1999: Study of Gulf Stream features with a multifrequency polarimetric SAR from the space shuttle. *IEEE. Trans. Geosci. Remote Sens.*, **37**, 2495–2507.
- Chunchuzov, I., P. W. Vachon, and X. Li, 2000: Analysis and modeling of atmospheric gravity waves observed in RADARSAT SAR images. *Remote Sens. Environ.*, **74**, 343–361.
- Clemente-Colòn, P., and X. H. Yan, 1999: Observations of east coast upwelling conditions in synthetic aperture radar imagery. *IEEE. Trans. Geosci. Remote Sens.*, **37**, 2239–2248.
- da Silva, J. C. B., S. A. Ermakov, I. S. Robinson, D. R. G. Jeans, and S. V. Kijashko, 1998: Role of surface films in ERS SAR signatures of internal waves on the shelf , 1, Short-period internal waves. *J. Geophys. Res.*, **103** (C4), 8009–8031.
- , ——, and ——, 2000: Role of surface films in ERS SAR signatures of internal waves on the shelf, 3, Mode transitions. *J. Geophys. Res.*, **105** (C10), 24 089–24 104.

- Dickey, T. D., 1991: The emergence of concurrent high resolution physical and biooptical measurements in the upper ocean and their applications. *Rev. Geophys.*, **29**, 383–413.
- DiGiacomo, P. M., and B. Holt, 2001: Satellite observations of small coastal ocean eddies in the Southern California Bight. *J. Geophys. Res.*, **106** (C10), 22 521–22 544.
- , L. Washburn, B. Holt, and B. H. Jones, 2004: Coastal pollution hazards in Southern California observed by SAR imagery: Stormwater plumes, wastewater plumes, and natural hydrocarbon seeps. *Marine Pollution Bulletin*, accepted.
- Dokken, S. T., R. Olsen, T. Wahl, and M. V. Tantillo, 2001: Identification and characterization of internal waves in SAR images along the coast of Norway. *Geophys. Res. Lett.*, **28**, 2803–2806.
- Donelan, M. A., and W. J. Pierson, 1987: Radar scattering and equilibrium ranges in wind-generated waves with application to scatterometry. *J. Geophys. Res.*, **92** (C5), 4971–5029.
- Dowd, M., P. W. Vachon, F. W. Dobson, and R. B. Olsen, 2001: Ocean wave extraction from RADARSAT synthetic aperture radar inter-look image cross-spectra. *IEEE Trans. Geosci. Remote Sens.*, **39**, 21–37.
- Elachi, C., 1978: Radar imaging of the ocean surface. *Bound.-Layer Meteor.*, **13**, 165–179.
- , 1987: *Introduction to the Physics and Techniques of Remote Sensing*. Wiley, 413 pp.
- , and J. Apel, 1976: Internal wave observations made with an airborne synthetic aperture imaging radar. *Geophys. Res. Lett.*, **3**, 647–650.
- , and W. E. Brown Jr., 1977: Models of radar imaging of ocean surface waves. *IEEE Trans. Antennas Propag.*, **25**, 84–95.
- , T. W. Thompson, and D. King, 1977: Ocean wave patterns under Hurricane Gloria: Observations with an airborne synthetic aperture radar. *Science*, **198**, 609–610.
- Engen, G., and H. Johnsen, 1995: SAR-ocean wave inversion using image cross spectra. *IEEE Trans. Geosci. Remote Sens.*, **33**, 1047–1056.
- Ermakov, S. A., J. C. B. da Silva, and I. S. Robinson, 1998: Role of surface films in ERS SAR signatures of internal waves on the shelf, 2, Internal tidal waves. *J. Geophys. Res.*, **103** (C4), 8033–8043.
- Espedal, H. A., and T. Wahl, 1999: Satellite SAR oil spill detection using wind history information. *Int. J. Remote Sens.*, **20**, 49–65.
- , O. M. Johannessen, and J. Knulst, 1996: Satellite detection of natural films on the ocean surface. *Geophys. Res. Lett.*, **23**, 3151–3154.
- , —, J. A. Johannessen, E. Dano, D. R. Lyzenga, and J. C. Knulst, 1998: COASTWATCH'95: ERS 1/2 SAR detection of natural film on the ocean surface. *J. Geophys. Res.*, **103**, 24 969–24 982.
- Feindt, F., V. Wismann, W. Alpers, and W. C. Keller, 1986: Airborne measurements of the ocean radar cross section at 5.3 GHz as a function of wind speed. *Radio Sci.*, **21**, 845–956.
- Fetterer, F., D. Gineris, and C. C. Wackerman, 1998: Validating a scatterometer wind algorithm for ERS-1 SAR. *IEEE Trans. Geosci. Remote Sens.*, **36**, 479–492.
- Fingas, M. F., and C. E. Brown, 1997: Review of oil spill remote sensing. *Spill Sci. Tech. Bull.*, **4**, 199–208.
- Frasier, S. J., and A. J. Camps, 2001: Dual-beam interferometry for ocean surface current vector mapping. *IEEE Trans. Geosci. Remote Sens.*, **39**, 401–414.
- Fu, L.-L., and B. Holt, 1982: Seasat views oceans and sea ice with synthetic-aperture radar. Jet Propulsion Laboratory Publ. 81-120, Pasadena, CA, 200 pp.

- , and —, 1983: Some examples of detection of oceanic mesoscale eddies by the Seasat synthetic-aperture radar. *J. Geophys. Res.*, **88**, 1844–1852.
- , and —, 1984: Internal waves in the Gulf of California from the Seasat synthetic-aperture radar. *J. Geophys. Res.*, **89**, 2053–2060.
- Gade, M., and W. Alpers, 1999: Using ERS-2 SAR images for routine observation of marine pollution in European coastal waters. *Sci. Total Environ.*, **238**, 441–448.
- , —, H. Hühnerfuss, H. Masuko, and T. Kobayashi, 1998a: Imaging of biogenic and anthropogenic ocean surface films by the multifrequency/multipolarization SIR-C/X-SAR. *J. Geophys. Res.*, **103** (C9), 18 851–18 866.
- , —, —, V. R. Wismann, and P. A. Lange, 1998b: On the reduction of the radar backscatter by oceanic surface films: Scatterometer measurements and their theoretical interpretation. *Remote Sens. Environ.*, **66**, 52–70.
- , —, S. A. Ermakov, H. Hühnerfuss, and P. A. Lange, 1998c: Wind-wave tank measurements of bound and freely propagating short gravity-capillary waves. *J. Geophys. Res.*, **103** (C10), 21 697–21 709.
- Gagliardini, D. A., P. Clemente-Colòn, J. Bava, J. A. Milovich, and L. A. Frulla, 2001: Complementary use of SAR and thermal IR observations in the Brazil–Malvinas confluence region. *Can. J. Remote Sens.*, **27**, 643–650.
- Gasparovic, R. F., J. R. Apel, and E. S. Kasischke, 1988: An overview of the SAR internal wave experiment. *J. Geophys. Res.*, **93** (C10), 12 304–12 316.
- Gerling, T. W., 1986: Structure of the surface wind field from the Seasat SAR. *J. Geophys. Res.*, **91**, 2308–2320.
- Goldstein, R. M., and H. A. Zebker, 1987: Interferometric radar measurement of ocean surface currents. *Nature*, **328**, 707–709.
- , T. P. Barnett, and H. A. Zebker, 1989: Remote sensing of ocean currents. *Science*, **246**, 1282–1285.
- Gonzalez, F. I., B. Holt, and D. G. Tilley, 1987: On the age and generation region of ocean swell observed in Hurricane Josephine. *Johns Hopkins APL Tech. Dig.*, **8**, 94–99.
- Graber, H. C., D. R. Thompson, and R. E. Carande, 1996: Ocean surface features and currents measured with synthetic aperture radar interferometry and HF radar. *J. Geophys. Res.*, **101** (C11), 25 813–25 832.
- Hasselmann, K., R. K. Raney, W. J. Plant, W. Alpers, R. A. Shuchman, D. R. Lyzenga, C. L. Rufenach, and M. J. Tucker, 1985: Theory of synthetic aperture radar ocean imaging: A MARSEN view. *J. Geophys. Res.*, **90** (C3), 4659–4686.
- Holt, B., 1988: Introduction: Studies of ocean wave spectra from the Shuttle Imaging Radar-B Experiment. *J. Geophys. Res.*, **93** (C12), 15 365–15 366.
- , 1998: Introduction to special section: Studies of the ocean surface from the Spaceborne Imaging Radar-C/X-Band SAR experiments. *J. Geophys. Res.*, **103** (C9), 18 813–18 814.
- , and J. Hilland, 2000: Rapid-repeat SAR imaging of the ocean surface: Are daily observations possible? *Johns Hopkins APL Tech. Dig.*, **21**, 162–169.
- , A. K. Liu, D. W. Wang, A. Gnanadesikan, and H. S. Chen, 1998: Tracking storm-generated waves in the northeast Pacific Ocean with ERS-1 synthetic aperture radar imagery and buoys. *J. Geophys. Res.*, **103** (C4), 7917–7930.
- Hornafius, J. S., D. Quigley, and B. P. Luyendyk, 1999: The world’s most spectacular marine hydrocarbon seeps (Coal Oil Point, Santa Barbara Channel, California): Quantification of emissions. *J. Geophys. Res.*, **104**, 20 703–20 711.

- Irvine, D. E., and D. G. Tilley, 1988: Ocean surface wave directional spectra and wave–current interaction from the Shuttle Imaging Radar-B synthetic aperture radar. *J. Geophys. Res.*, **93** (C12), 15 389–15 401.
- Jameson, A. R., F. K. Li, S. L. Durden, Z. S. Haddad, B. Holt, T. Fogarty, and R. K. Moore, 1997: SIR-C/X-SAR observations of rain storms. *Remote Sens. Environ.*, **59**, 267–279.
- Johannessen, J. A., R. A. Shuchman, O. M. Johannessen, K. L. Davidson, and D. R. Lyzenga, 1991: Synthetic aperture radar imaging of upper ocean circulation and wind fronts. *J. Geophys. Res.*, **96**, 10 411–10 422.
- , G. Digranes, H. Espedal, O. M. Johannessen, and P. Samuel, 1994: SAR ocean feature catalogue. European Space Agency Publications ESA SP-1174, 106 pp.
- , R. A. Shuchman, G. Digranes, D. Lyzenga, C. Wackerman, O. M. Johannessen, and P. W. Vachon, 1996: Coastal ocean fronts and eddies imaged with ERS-1 synthetic aperture radar. *J. Geophys. Res.*, **101**, 6651–6667.
- Jones, B., 2001: A comparison of visual observations of surface oil with synthetic aperture radar imagery of the Sea Empress oil spill. *Int. J. Remote Sens.*, **22**, 1619–1638.
- Katsaros, K. B., P. W. Vachon, W. T. Liu, and P. G. Black, 2002: Microwave remote sensing of tropical cyclones from space. *J. Oceanogr.*, **58**, 137–151.
- Kinsman, B., 1984: *Wind Waves*. Dover, 676 pp.
- Korsbakken, E., J. A. Johannessen, and O. M. Johannessen, 1998: Coastal wind field retrievals from ERS synthetic aperture radar. *J. Geophys. Res.*, **103** (C4), 7857–7874.
- Lee, J.-S., R. W. Jansen, D. L. Schuler, T. L. Ainsworth, G. Marmorino, and S. Chubb, 1998: Polarimetry analysis and modeling of multifrequency SAR signatures from Gulf Stream fronts. *IEEE J. Oceanic Eng.*, **23**, 322–333.
- Lehner, S., J. Horstmann, W. Koch, and W. Rosenthal, 1998: Mesoscale wind measurements using recalibrated ERS SAR images. *J. Geophys. Res.*, **103** (C4), 7847–7856.
- Levy, G., 2001: Boundary layer roll statistics from SAR. *Geophys. Res. Lett.*, **28**, 1993–1995.
- Lichy, D. E., M. G. Mattie, and L. J. Mancini, 1981: Tracking of a warm water ring. *Spaceborne Synthetic Aperture Radar for Oceanography*, R. C. Beal, P. S. DeLeonibus, and I. Katz, Eds., The Johns Hopkins University Press, 171–182.
- Li, X. F., P. Clemente-Colòn, and K. S. Friedman, 2000: Estimating oceanic mixed-layer depth from internal wave evolution observed from RADARSAT-1 SAR. *Johns Hopkins APL Tech. Dig.*, **21**, 130–135.
- , P. Clemente-Colòn, W. G. Pichel, and P. W. Vachon, 2000: Atmospheric vortex streets on a RADARSAT SAR image. *Geophys. Res. Lett.*, **27**, 1655–1658.
- Lin, I. I., W. Alpers, V. Khoo, H. Lim, T. K. Lim, and D. Kasilingam, 2001: An ERS-1 synthetic aperture radar image of a tropical squall line compared with weather radar data. *IEEE Trans. Geosci. Remote Sens.*, **39**, 937–945.
- Liss, P. S., and R. A. Duce, 1997: *The Sea Surface and Global Change*. Cambridge University, 519 pp.
- Liu, A. K., 1988: Analysis of nonlinear internal waves in the New York Bight. *J. Geophys. Res.*, **93** (C10), 12 317–12 329.
- , C. Y. Peng, and J. D. Shumacher, 1994: Wave–current interaction study in the Gulf of Alaska for the detection of eddies by synthetic aperture radar. *J. Geophys. Res.*, **99** (C5), 10 075–10 085.
- , Y. S. Chang, M. K. Hsu, and N. K. Liang, 1998: Evolution of nonlinear internal waves in the East and South China Seas. *J. Geophys. Res.*, **103** (C4), 7995–8008.

- Lu, J., L. K. Kwok, H. Lim, S. C. Liew, and M. Bao, 2000: Mapping oil pollution from space. *Backscatter*, **11**, 23-26.
- Lyzenga, D. R., 1991: Interaction of short surface and electromagnetic waves with ocean fronts. *J. Geophys. Res.*, **96**, 10 765–10 772.
- , 1998: Effects of intermediate-scale waves on radar signatures of ocean fronts and internal waves. *J. Geophys. Res.*, **103** (C9), 18 759–18 768.
- , and J. R. Bennett, 1988: Full-spectrum modeling of synthetic aperture radar internal wave signatures. *J. Geophys. Res.*, **93** (C10), 12 345–12 354.
- , and G. O. Marmorino, 1998: Measurement of surface currents using sequential synthetic aperture radar images of slicks patterns near the edge of the Gulf Stream. *J. Geophys. Res.*, **103** (C9), 18 769–18 777.
- MacDonald, I. R., N. L. Guinasso, S. G. Ackleson, J. F. Amos, R. Duckworth, and J. M. Brooks, 1993: Natural oil slicks in the Gulf of Mexico visible from space. *J. Geophys. Res.*, **98** (C9), 16 351–16 364.
- Marmorino, G. O., D. R. Thompson, H. C. Graber, and C. L. Trump, 1997: Correlation of oceanographic signatures appearing in synthetic aperture radar and interferometric synthetic aperture radar imagery with in situ measurements. *J. Geophys. Res.*, **102** (C8), 18 723–18 736.
- , D. R. Lyzenga, and J. A. C. Kaiser, 1999: Comparison of airborne synthetic aperture radar imagery with in situ surface-slope measurements across Gulf Stream slicks and a convergent front. *J. Geophys. Res.*, **104** (C1), 1405–1422.
- Marom, M., L. Shemer, and E. B. Thornton, 1991: Energy density directional spectra of a nearshore wave field measured by interferometric synthetic aperture radar. *J. Geophys. Res.*, **96** (C12), 22 125–22 134.
- Martin, S., 2004: *Introduction to Ocean Remote Sensing*. Cambridge University Press, (In Press).
- , K. Steffen, J. Comiso, D. Cavalieri, M. Drinkwater, and B. Holt, 1992: Microwave remote sensing of polynyas. *Microwave Remote Sensing of Sea Ice*, F. Carsey, Ed., Amer. Geophys. Union, Washington, DC, 303–311.
- Martinez-Diaz-de-Leon, A., I. S. Robinson, D. Ballesteros, and E. Coen, 1999: Wind driven circulation features in the Gulf of Tehuantepec, Mexico, revealed by combined SAR and SST satellite sensor data. *Int. J. Remote Sens.*, **20**, 1661–1668.
- Melsheimer, C., W. Alpers, and M. Gade, 1998: Investigation of multifrequency/multipolarization radar signatures of rain cells over the ocean using SIR-C/X-SAR data. *J. Geophys. Res.*, **103** (C9), 18 867–18 884.
- , ———, and ———, 2001: Simultaneous observations of rain cells over the ocean by the synthetic aperture radar aboard the ERS satellites and by surface-based weather radars. *J. Geophys. Res.*, **106** (C3), 4665–4677.
- Moccia, A., and G. Ruffino, 2001: Spaceborne along-track SAR interferometry: Performance analysis and mission scenarios. *IEEE Trans. Aerosp. Electron. Syst.*, **37**, 199–213.
- Moller, D., S. J. Frasier, D. L. Porter, and R. E. McIntosh, 1998: Radar-derived interferometric surface currents and their relationship to subsurface current structure. *J. Geophys. Res.*, **103** (C6), 12 839–12 852.
- Mollo-Christensen, E., 1981: Surface signs of internal ocean dynamics. *Spaceborne Synthetic Aperture Radar for Oceanography*, R. C. Beal, P. S. DeLeonibus, and I. Katz, Eds., The Johns Hopkins University Press, 140–145.

- Monaldo, F. M., D. R. Thompson, R. C. Beal, W. G. Pichel, and P. Clemente-Colòn, 2001: Comparison of SAR-derived wind speed with model predictions and ocean buoy measurements. *IEEE Trans. Geosci. Remote Sens.*, **39**, 2587–2600.
- Moore, R. K., A. Mogili, Y. Fang, B. Beh, and A. Ahamad, 1997: Rain measurement with SIR-C/X-SAR. *Remote Sens. Environ.*, **59**, 280–293.
- Mourad, P. D., 1996: Inferring multiscale structure in atmospheric turbulence using satellite-based synthetic aperture radar imagery. *J. Geophys. Res.*, **101**, 18 433–18 499.
- , and B. A. Walter, 1996: Viewing a cold air outbreak using satellite-based synthetic aperture radar and advanced very high resolution radiometer imagery. *J. Geophys. Res.*, **101**, 16 391–16 400.
- , D. R. Thompson, and D. C. Vandemark, 2000: Extracting fine-scale wind fields from synthetic aperture radar images of the ocean surface. *Johns Hopkins APL Tech. Dig.*, **21**, 108–115.
- Munk, W., L. Armi, K. Fischer, and F. Zachariasen, 2000: Spirals on the sea. *Proc. Roy. Soc. London*, **A456**, 1217–1280.
- Neumann, G., and W. J. Pierson, 1966: *Principles of Physical Oceanography*. Prentice-Hall, 545 pp.
- Nilsson, C. S., and P. C. Tildesley, 1995: Imaging of oceanic features by ERS-1 synthetic aperture radar. *J. Geophys. Res.*, **100**, 953–967.
- Pan, F., and R. B. Smith, 1999: Gap winds and wakes: SAR observations and numerical simulation. *J. Atmos. Sci.*, **56**, 905–923.
- Pavlakakis, P., D. Tarchi, and A. J. Sieber, 2001: On the monitoring of illicit vessel discharges using spaceborne SAR remote sensing—A reconnaissance study in the Mediterranean sea. *Ann. Telecommun.*, **56**, 700–718.
- Pichel, W. G., and P. Clemente-Colòn, 2000: NOAA CoastWatch SAR applications and demonstration. *Johns Hopkins APL Tech. Dig.*, **21**, 49–57.
- Plant, W. J., 1990: Bragg scattering of electromagnetic waves from the air/sea interface. *Surface Waves and Fluxes*, G. L. Geernaert and W. J. Plant, Eds., Vol. 2, Kluwer Academic Publishers, 41–108.
- , 1997: A model for microwave Doppler sea return at high incidence angles: Bragg scattering from bound, tilted waves. *J. Geophys. Res.*, **102** (C9), 21 131–21 146.
- , 2002: A stochastic, multiscale model of microwave backscatter from the ocean. *J. Geophys. Res.*, **107**, 3120, doi:10.1029/2001JC000909.
- , E. A. Terray, R. A. Petitt, and W. C. Keller, 1994: The dependence of microwave backscatter from the sea on illuminated area-correlation times and lengths. *J. Geophys. Res.*, **99** (C5), 9705–9723.
- Porter, D. L., and D. R. Thompson, 1999: Continental shelf parameters inferred from SAR internal wave observations. *J. Atmos. Oceanic Technol.*, **16**, 475–487.
- Raney, R. K., 1998: Radar fundamentals: Technical perspective. *Principles and Applications of Imaging Radar, Manual of Remote Sensing*, F. M. Henderson and A. J. Lewis, Eds., Vol. 2., 3d. ed., Wiley, 9–130.
- Robinson, I., 1997: Remote sensing of the sea-surface microlayer. *The Sea Surface and Global Change*, P. S. Liss and R. A. Duce, Eds., Cambridge University Press, pp.471-508
- Rodriguez, E., B. D. Pollard, and J. M. Martin, 2003: Wide swath ocean altimetry using radar interferometry. *IEEE Trans. Geosci. Remote Sens.*, in press.

- Romeiser, R., and W. Alpers, 1997: An improved composite surface model for the radar backscattering cross section of the ocean surface, 2, Model response to surface roughness variations and the radar imaging of underwater bottom topography. *J. Geophys. Res.*, **102** (C11), 25 251–25 267.
- , and D. R. Thompson, 2000: Numerical study on the along-track interferometric radar imaging mechanism of oceanic surface currents. *IEEE. Trans. Geosci. Remote Sens.*, **38**, 446–458.
- , W. Alpers, and V. Wismann, 1997: An improved composite surface model for the radar backscattering cross section of the ocean surface, 1, Theory of the model and optimization/validation by scatterometer data. *J. Geophys. Res.*, **102** (C11), 25 537–25 250.
- Ross, D. B., 1981: The wind speed dependency of ocean microwave backscatter. *Spaceborne Synthetic Aperture Radar for Oceanography*, R. C. Beal, P. S. DeLeonibus, and I. Katz, Eds., The Johns Hopkins University Press, 75–86.
- Schuler, D. L., J.-S. Lee, and K. W. Hoppel, 1993: Polarimetric SAR image signatures of the ocean and Gulf Stream features. *IEEE. Trans. Geosci. Remote Sens.*, **31**, 1210–1221.
- Schulz-Stellenfleth, J., J. Horstmann, S. Lehner, and W. Rosenthal, 2001: Sea surface imaging with an across-track synthetic aperture radar: The SINEWAVE experiment. *IEEE. Trans. Geosci. Remote Sens.*, **39**, 2017–2028.
- Shemer, L., and M. Marom, 1993: Estimates of ocean coherence time by an interferometric SAR. *Int. J. Remote Sens.*, **14**, 3021–3029.
- Shimada, T., H. Kawamura, and M. Shimada, 2003: An L-band geophysical model function for SAR wind retrieval using JERS-1 SAR. *IEEE Trans. Geosci. Remote Sens.*, **41**(3), 518–531.
- Sikora, T. D., and D. R. Thompson, 2002: Air-sea turbulence statistics from synthetic aperture radar: An update. *Can. J. Remote Sens.*, **28**, 517–523.
- , G. S. Young, R. C. Beal, and J. B. Edson, 1995: Use of spaceborne synthetic aperture radar imagery of the sea surface in detecting the presence and structure of the convective marine atmospheric boundary layer. *Mon. Wea. Rev.*, **123**, 3623–3632.
- , H. N. Shirer, and R. D. Chapman, 1997: Estimating convective atmospheric boundary layer depth from microwave radar imagery of the sea surface. *J. Appl. Meteor.*, **36**, 833–845.
- , K. S. Friedman, W. G. Pichel, and P. Clemente-Colòn, 2000: Synthetic aperture radar as a tool for investigating polar mesoscale cyclones. *Wea. Forecasting*, **15**, 745–758.
- Solberg, A. H. S., G. Storvik, R. Solberg, and E. Volden, 1999: Automatic detection of oil spills in ERS SAR images. *IEEE Trans. Geosci. Remote Sens.*, **37**, 1916–1924.
- Stewart, R., 1985: *Methods of Satellite Oceanography*. University of California, 360 pp.
- Stoffelen, A., and D. Anderson, 1997: Scatterometer data interpretation: Estimation and validation of the transfer function CMOD4. *J. Geophys. Res.*, **102** (C3), 5767–5780.
- Svejkovsky, J., and B. Jones, 2001: Satellite imagery detects coastal stormwater and sewage runoff. *Eos, Trans. Amer. Geophys. Union*, **82**, 621, 624–625, 630.
- Thompson, D. R., 1988: Calculation of radar backscatter modulations from internal waves. *J. Geophys. Res.*, **93** (C10), 12 371–12 380.
- , and J. R. Jensen, 1993: Synthetic aperture radar interferometry applied to ship-generated internal waves in the 1989 Loch Linnhe experiment. *J. Geophys. Res.*, **98** (C6), 10 259–10 269.
- , and R. C. Beal, 2000: Mapping high-resolution wind fields using synthetic aperture radar. *Johns Hopkins APL Tech. Dig.*, **21**, 58–67.

- , F. M. Monaldo, R. C. Beal, N. S. Winstead, W. G. Pichel, and P. Clemente-Colón, 2001: Combined estimates improve high-resolution coastal wind mapping. *EOS, Trans. Amer. Geophys. Union*, **82**, 469, 473-474.
- Trivero, P., B. Fiscella, F. Gomez, and P. Pavese, 1998: SAR detection and characterization of sea surface slicks. *Int. J. Remote Sens.*, **19**, 543-548.
- Ufermann, S., and R. Romeiser, 1999: A new interpretation of multifrequency/multipolarization radar signatures of the Gulf Stream front. *J. Geophys. Res.*, **104** (C11), 25 697–25 705.
- Ulaby, F. T., R. K. Moore, and A. K. Fung, 1982: *Microwave Remote Sensing: Active and Passive*. Vol. 1. Addison-Wesley, pp. 1 - 456
- , ——, and ——, 1982: *Microwave Remote Sensing: Active and Passive*. Vol. 2. Addison-Wesley, pp. 457-1064
- , ——, and ——, 1986: *Microwave Remote Sensing: Active and Passive*. Vol. 3. Artech House, pp. 1065-2126
- Unal, C. M. H., P. Snoeig, and P. J. F. Swart, 1991: The polarization-dependent relation between radar backscatter from the ocean surface and surface wind vector at frequencies between 1 and 18 GHz. *IEEE Trans. Geosci. Remote Sens.*, **29**, 621–626.
- Vachon, P. W., and F. W. Dobson, 2000: Wind retrieval from RADARSAT SAR images: Selection of a suitable C-band HH polarization wind retrieval model. *Can. J. Remote Sens.*, **26**, 306–313.
- , O. M. Johannessen, and J. A. Johannessen, 1994: An ERS 1 synthetic aperture radar image of atmospheric lee waves. *J. Geophys. Res.*, **99**, 22 483–22 490.
- , J. W. M. Campbell, A. L. Gray, and F. W. Dobson, 1999: Validation of along-track interferometric SAR measurements of ocean surface waves. *IEEE. Trans. Geosci. Remote Sens.*, **37**, 150–162.
- Valenzuela, G. R., 1978: Theories for the interaction of electromagnetic and ocean waves—A review. *Bound.-Layer Meteor.*, **13**, 61–85.
- Vandemark, D., P. D. Mourad, S. A. Bailey, T. L. Crawford, C. A. Vogel, J. Sun, and B. Chapron, 2001: Measured changes in ocean surface roughness due to atmospheric boundary layer rolls. *J. Geophys. Res.*, **106** (C3), 4639–4654.
- van Zyl, J. J., H. A. Zebker, and C. Elachi, 1987: Imaging radar polarization signatures: Theory and observations. *Radio Sci.*, **22**, 529–543.
- Vesecky, J. F., and R. H. Stewart, 1982: Observations of the sea surface phenomena using imagery from the Seasat synthetic aperture radar: An assessment. *J. Geophys. Res.*, **87**, 3397–3430.
- Vogelzang, J., 1997: Mapping submarine sand waves with multiband imaging radar. 1. Model development and sensitivity analysis. *J. Geophys. Res.*, **102** (C1), 1163–1181.
- , G. J. Wensink, C. J. Calkoen, and M. W. A. VanderKooij, 1997: Mapping submarine sand waves with multiband imaging radar. 2. Experimental results and model comparison. *J. Geophys. Res.*, **102** (C1), 1183–1192.
- Wackerman, C. C., C. L. Rufenach, R. A. Shuchman, J. A. Johannessen, and K. L. Davidson, 1996: Vector retrieval using ERS-1 synthetic aperture radar imagery. *IEEE Trans. Geosci. Remote Sens.*, **34**, 1343–1352.
- , P. Clemente-Colón, W. G. Pichel, and X. F. Li, 2002: A two-scale model to predict C-band VV and HH normalized radar cross section values over the ocean. *Can J. Remote Sens.*, **28**, 367–384.

SAR Imaging of the Ocean Surface

- Winstead, N. S., and P. D. Mourad, 2000: Shallow Great Lake-scale atmospheric thermal circulation imaged by synthetic aperture radar. *Mon. Wea. Rev.*, **128**, 3654–3663.
- , and G. S. Young, 2000: An analysis of exit-flow drainage jets over the Chesapeake Bay. *J. Appl. Meteor.*, **39**, 1269–1281.
- , T. D. Sikora, D. R. Thompson, and P. D. Mourad, 2002: Direct influence of gravity waves on surface-layer stress during a cold air outbreak, as shown by synthetic aperture radar. *Mon. Wea. Rev.*, **130**, 2764–2776.
- Wismann, V., M. Gade, W. Alpers, and H. Huhnerfuss, 1998: Radar signatures of marine mineral oil spills measured by an airborne multi-frequency radar. *Int. J. Remote Sens.*, **19**, 3607–3623.
- Worthington, R. M., 2001: Alignment of mountain lee waves viewed using NOAA AVHRR imagery, MST radar, and SAR. *Int. J. Remote Sens.*, **22**, 1361–1374.
- Young, G., 2000: SAR signatures of the marine atmospheric boundary layer: Implications for numerical forecasting. *Johns Hopkins APL Tech. Dig.*, **21**, 27–32.
- Zebker, H. A., J. J. van Zyl, S. L. Durden, and L. Norikane, 1991: Calibrated imaging radar polarimetry: Techniques, examples, and applications. *IEEE Trans. Geosci. Remote Sens.*, **29**, 942–961.
- Zheng, Q. N., X. H. Yan, V. Klemas, C.R. Ho, N. J. Kuo, and Z. M. Wang, 1998: Coastal lee waves on ERS-1 SAR images. *J. Geophys. Res.*, **103** (C4), 7979–7993.
- , Y. L. Yuan, V. Klemas, and X. H. Yan, 2001: Theoretical expression for an ocean internal soliton synthetic aperture radar image and determination of the soliton characteristic half width. *J. Geophys. Res.*, **106** (C12), 31 415–31 423.